LLNL-JRNL-412903

LAWRENCE
LIVERMORE
NATIONAL
LABORATORY

Finite-Temperature Non-equilibrium Quasicontinuum Method based on Langevin Dynamics

J. Marian, G. Venturini, B. Hansen, J. Knap, M. Ortiz, G. Campbell

May 11, 2009

Modelling and Simulation in Materials Science and Engineering

Disclaimer

This document was prepared as an account of work sponsored by an agency of the United States government. Neither the United States government nor Lawrence Livermore National Security, LLC, nor any of their employees makes any warranty, expressed or implied, or assumes any legal liability or responsibility for the accuracy, completeness, or usefulness of any information, apparatus, product, or process disclosed, or represents that its use would not infringe privately owned rights. Reference herein to any specific commercial product, process, or service by trade name, trademark, manufacturer, or otherwise does not necessarily constitute or imply its endorsement, recommendation, or favoring by the United States government or Lawrence Livermore National Security, LLC. The views and opinions of authors expressed herein do not necessarily state or reflect those of the United States government or Lawrence Livermore National Security, LLC, and shall not be used for advertising or product endorsement purposes.

Finite-Temperature Non-equilibrium Quasicontinuum Method based on Langevin Dynamics

J Marian[1], G Venturini[2], BL Hansen[2], J Knap[3], M Ortiz[2], GH Campbell[1]

[1]Physical and Life Sciences Directorate, Lawrence Livermore National Laboratory, Livermore, CA 94551, USA
[2]Division of Engineering and Applied Science, California Institute of Technology, Pasadena, CA 91125, USA
[3]US Army Research Laboratory, Aberdeen Proving Ground, MD 21005, USA

E-mail: `marian1@llnl.gov`

Abstract. The concurrent bridging of molecular dynamics and continuum thermodynamics presents a number of challenges, mostly associated with energy transmission and changes in the constitutive description of a material across domain boundaries. In this paper, we propose a framework for simulating coarse dynamic systems in the canonical ensemble using the Quasicontinuum method (QC). The equations of motion are expressed in reduced QC coordinates and are strictly derived from dissipative Lagrangian mechanics. The derivation naturally leads to a classical Langevin implementation where the timescale is governed by vibrations emanating from the finest length scale occurring in the computational cell. The equations of motion are integrated explicitly via Newmark's ($\beta = 0; \gamma = \frac{1}{2}$) method, leading to a robust numerical behavior and energy conservation. In its current form, the method only allows for wave propagations supported by the less compliant of the two meshes across a heterogeneous boundary, which requires the use of overdamped dynamics to avoid spurious heating due to reflected vibrations. We have applied the method to two independent crystallographic systems characterized by different interatomic potentials (Al and Ta) and have measured thermal expansion in order to quantify the vibrational entropy loss due to homogenization. We rationalize the results in terms of system size, mesh coarseness, and nodal cluster diameter within the framework of the quasiharmonic approximation. For Al, we find that the entropy loss introduced by mesh coarsening varies linearly with the element size, and that volumetric effects are not critical in driving the anharmonic behavior of the simulated systems. In Ta, the anomalies of the interatomic potential employed result in negative and zero thermal expansion at low and high temperatures, respectively.

1. Introduction.

Molecular dynamics (MD) provides a straightforward way to simulate thermally activated processes and field gradient-driven effects, including heat and mass transport. However, the characteristic time of MD is that of atomic vibrations, which limits the time and length scales accessible by direct simulation. Alternatively, when fields are smoothly varying, the configurational space can be discretized into finite elements (FE), where the reduced set of degrees of freedom (DOF) is the ensemble of element vertices and the material laws are continuum in nature. This nodal representation results in reduced computational overhead which can be directed to sampling larger time and space scales.

In the presence of abrupt gradients, the FE method takes recourse to mesh refinement to improve the discrete representation of the elastic energy integrals for a continuous medium. However, when the mesh size approaches the atomistic limit, the constitutive relations are no longer valid, for they fail to capture the localized nature of the elastic energy functional. To circumvent this difficulty, combined atomistic/continuum approaches that use atomistic material descriptions where fields are non-linear, such as atomic-sized defects, while maintaining a coarse description elsewhere, have been developed [1, 2]. In this fashion, the computational power is harnessed according to the complexity of the material laws, resulting in an optimum compromise between numerical accuracy and computational overhead. Compared to direct atomistics, these techniques have the potential to produce significant time and length scale gains by treating smoothly-varying regions of the configurational space collectively.

When using these methods, the existence of unstructured meshes during dynamic simulations gives rise to coupled domain boundaries separating portions of the configurational space with different resolutions. In such cases, interfaces may become non-compliant from a thermodynamic point of view, which results from the fact that continuum thermodynamics is formulated as a lengthscale-free theory, and cannot account for the discreticity associated with meshes of varying coarseness. As a consequence, time-dependent information may not be seamlessly transmitted, and the dynamic behavior across both sides of an interface is governed by the reflection of waves not supported by the domain of coarser description (and the transmission of those that are). While they may not generally be important at low temperatures for smoothly-discretized meshes, these effects are accentuated at resolutions that approach the atomistic scale at finite temperatures, a common occurrence in many situations of interest. This can lead to spurious thermodynamic behaviors, with thermal gradients and other artifacts originating from inhomogenous boundaries. The most patent effect is the unphysical heating of domains suffering reflections [3, 2, 4]. This complication is not trivially solved, and, again, stems from the inherent quantization of lattice phonons and the development of impedance discontinuities across coupled-domain boundaries. This is inherent to space discretization methods, and has not been strictly solved even in FE [5, 6]. This is why there are rules of thumb for how fast the element size can be increased during mesh transition, and artificial bulk viscosities to impose viscous damping are used in methods such as finite elements and finite differences (*e.g.*, ref. [7]).

Techniques that resolve this limitation in the context of atomistic/continuum-bridging methods have been developed by, *e.g.*, Cai *et al* [8] and E and Zhongyi [9] using memory kernel functions and modified boundary hamiltonians for interface atoms, respectively. However, both approaches have proven exceedingly demanding computationally, and have not been applied beyond simple proof-of-concept cases. Recently, more computationally-benign methods that minimize transmission impedances have been proposed. For example, Park *et al* [10] have derived more compact time-history kernels for 2D simulations, resulting in 'bidirectional' dynamics that filter lattice waves automatically. Another noteworthy technique is the coarse-grained molecular dynamics (CGMD) method of Rudd and Broughton [4], which has been constructed to provide a consistent treatment of the short wavelength modes which are present in the underlying atomistics but are missing from the coarse finite element mesh. In CGMD, the short wavelength modes missing from the mesh are taken to be in thermal equilibrium, and their average contribution is included in the dynamics of the system. Others, such as Curtarolo and Ceder [11] and Wagner *et al* [12], have proposed techniques to model thermal flow across heterogeneous boundaries, whereby all impinging waves contribute to the temperature fields of boundary nodes, which are smoothly transmitted to finite-element regions. However, phonons do reflect without being explicitly removed from the system, which in certain temperature ranges could lead to unphysical heating. Methods that take into account the lost entropy from the missing DOF in atomistic/continuum representations have been proposed for equilibrium thermodynamics simulations [13, 14, 15, 16, 17]. These approaches succeed in computing full thermodynamic averages across domains although they suppress local thermal fluctuations and cannot be applied to compute transport phenomena.

Here we develop an approach similar to that of Qu *et al* [18] within the Quasicontinuum (QC) framework [19, 20]. We take advantage of the seamless bridging of length scales furnished by the QC formulation to write the equations of motion in terms of dissipative Lagrangian mechanics, with a viscous term that expends the thermal energy introduced by a Langevin thermostat through a suitable random force at the nodal level. Unlike Qu *et al*, however, the renormalization procedure does not depend on the element size or position, only the parameterization does, which emanates naturally from QC's kinematic constraints. In other words, the equations of motion have the same form across the entire domain and are simply scaled by a nodal mass-weighed viscosity. In this fashion, phonons not transmitted across mesh boundaries are dampened in accordance with the imposed thermostat so as to sample stable canonical ensemble trajectories. Our method is fully anharmonic and can be used to study non-equilibrium, thermally-activated processes directly. However, impoverished phonon spectra in coarse regions result in an underestimation of thermal properties such as thermal expansion, specific heat capacities, etc. It is important to understand and quantify this loss of entropy stemming from length scale inhomogeneities.

Quantifying the loss of information across domain interfaces is generally done in terms of reflection coefficients involving characteristic impedances [4, 8]. A more direct way is by computing entropic losses via the Debye-Grüneisen model (quasiharmonic approximation) [21, 22, 16] or some other thermodynamic integration methods [23]. The thermal expansion coefficient α is generally taken as a good metric to measure entropy loss, as all frequencies participate in thermal expansion, especially those most sensitive to volume changes. Here, we study the thermal expansion behavior of two metallic systems, one face-centered cubic (fcc) —Al—, one body-centered cubic (bcc) —Ta—, described by standard embedded-atom method (EAM) potentials. We quantify entropic losses in coarse meshes and express α in terms of QC's critical parameters. We rationalize the results in terms of the mesh and cluster size effects on the system eigenfrequencies and propose rescaling strategies for coarse and inhomogeneous systems.

This paper is organized as follows: Section 2 provides a concise review of QC and the general framework for dissipative Lagrangian mechanics. An equation of motion is then derived for the reduced DOF subset, and methods for solving it are discussed. In Section 3, the details of the computational implementation are given, with emphasis on the selection of a stability-ensuring parameterization. Section 4 contains all the dynamic results and their interpretation within the quasiharmonic approximation for both materials. Finally, in Section 5 we present a brief discussion of the method and the implications of our results and provide the conclusions of our work.

2. Theory.

2.1. Zero-temperature Quasicontinuum.

To provide the background for subsequent developments, we briefly review the static QC theory developed by Tadmor *et al* [19] and its adaptation by Knap and Ortiz [20]. We consider a set of N atoms occupying a subset of a simple d-dimensional Bravais lattice defined by lattice vectors $\boldsymbol{a}_i,\ i = 1, ..., d$. The coordinates of the atoms in the reference configuration of the crystal are:

$$\boldsymbol{X}(\boldsymbol{l}) = \sum_{i=1}^{d} l_i \boldsymbol{a}_i,\ \boldsymbol{l} \in \mathcal{L} \subset \mathbb{Z}^d \tag{1}$$

where $\boldsymbol{l}$ denotes the discrete lattice coordinates and $\mathbb{Z}$ is the set of integer numbers. The corresponding atomic coordinates in the deformed configuration are $\boldsymbol{q} = \{\boldsymbol{q}(\boldsymbol{l}),\ \boldsymbol{l} \in \mathcal{L}\} \in X$. The linear space $X \equiv \mathbb{R}^{Nd}$ may be referred to as the *configuration* space of the crystal. The energy of the crystal is assumed to be expressible as a function of the atomic coordinates, $E(\boldsymbol{q})$. Moreover, any applied loads are considered conservative and derived from an external potential $\Phi^{\text{ext}}(\boldsymbol{q})$. Therefore, the total potential energy of the crystal is:

$$\Phi(\boldsymbol{q}) = E(\boldsymbol{q}) + \Phi^{\text{ext}}(\boldsymbol{q}) \tag{2}$$

The stable equilibrium configurations of interest are the minimizers of this function over the space X, *i.e.* the solutions to the variational problem:

$$\min_{\boldsymbol{q}\in X} \Phi(\boldsymbol{q}) \tag{3}$$

The essence of the QC method is to replace eq. (3) by a constrained minimization of $\Phi(\boldsymbol{q})$ over a suitably chosen subspace $X_h \subset X$. To define X_h we begin by selecting a reduced set $\mathcal{L}_h \subset \mathcal{L}$ containing $N_h < N$ *representative* atoms. Additionally, let $\mathcal{T}_h$ be a triangulation of $\mathcal{L}_h$ and suppose that the crystal lattice $\mathcal{L}$ is contained within a polytope of $\mathcal{L}_h$ (which in general need not be a Bravais lattice†). The triangulation $\mathcal{T}_h$ supports a collection of shape functions, $\{\varphi_h(\boldsymbol{l}|\boldsymbol{l}_h),\ \boldsymbol{l}_h \in \mathcal{T}_h\}$. The $\varphi_h(\boldsymbol{l}|\boldsymbol{l}_h)$ are continuous and piecewise linear and their domain is restricted to the simplices K of the triangulation $\mathcal{T}_h$, *i.e.* they take a value of unity at $\boldsymbol{l}_h$ and vanish elsewhere. The positions of all atoms in $\mathcal{L}$ can then be determined by interpolation of the coordinates of all $\boldsymbol{l}_h \in \mathcal{L}_h$, namely:

$$\boldsymbol{q}(\boldsymbol{l}) = \sum_{\boldsymbol{l}_h\in\mathcal{L}_h} \varphi_h(\boldsymbol{l}|\boldsymbol{l}_h)\boldsymbol{q}_h(\boldsymbol{l}_h) \tag{4}$$

where $\boldsymbol{q}_h = \{\boldsymbol{q}_h(\boldsymbol{l}_h),\ \boldsymbol{l}_h \in \mathcal{L}_h\}$ is an array containing the nodal coordinates in the deformed configuration of the crystal —the spatial nodal coordinates—, *i.e.* an element of the linear space X_h of reduced dimension $N_h d$ (cf. [20]).

The reduced counterpart of eq. (3) then becomes:

$$\min_{\boldsymbol{q}_h\in X_h} \Phi(\boldsymbol{q}_h) \tag{5}$$

The minimizers of the reduced problem follow from the reduced equations of equilibrium:

$$\boldsymbol{f}_h(\boldsymbol{l}_h) = \sum_{\boldsymbol{l}\in\mathcal{L}} \boldsymbol{f}(\boldsymbol{l}|\boldsymbol{q}_h)\varphi_h(\boldsymbol{l}|\boldsymbol{l}_h) = 0 \tag{6}$$

where $\boldsymbol{f}(\boldsymbol{q}) = \Phi_{,\boldsymbol{q}}(\boldsymbol{q})$ are the forces corresponding to $\boldsymbol{q}$ and $\boldsymbol{f}(\boldsymbol{l}|\boldsymbol{q})$ is the value of $\boldsymbol{f}(\boldsymbol{q})$ at site $\boldsymbol{l}$.

As noted by Tadmor *et al* [19], however, the practicality of the method hinges on the application of lattice summation rules in order to avoid the calculation of the full atomistic force array $\boldsymbol{f}$. Following Knap and Ortiz [20], cluster summation rules are used as a compromise between numerical accuracy and computational efficiency. Clusters are defined as $\mathcal{C}(\boldsymbol{l}_h) = \{\boldsymbol{l} : |\boldsymbol{X}(\boldsymbol{l}) - \boldsymbol{X}(\boldsymbol{l}_h)| \leq r_c(\boldsymbol{l}_h)\}$, where $r_c(\boldsymbol{l}_h)$ is the radius of a sphere centered on a representative atom $\boldsymbol{l}_h$. The application of the cluster summation rule to the reduced equilibrium equations (6) yields:

$$\boldsymbol{f}_h(\boldsymbol{l}_h) \approx \sum_{\boldsymbol{l}'_h\in\mathcal{L}_h} n_h(\boldsymbol{l}'_h)\left[\sum_{\boldsymbol{l}\in\mathcal{C}_h(\boldsymbol{l}'_h)} \boldsymbol{f}(\boldsymbol{l}|\boldsymbol{l}_h)\varphi_h(\boldsymbol{l}|\boldsymbol{l}_h)\right] = 0 \tag{7}$$

---

† The selection of these representative atoms is rather arbitrary, although procedures have been devised within the QC framework to factor $\mathcal{T}_h$ directly into the formulation of the energetics of the crystal [24].

where $n_h(\boldsymbol{l}_h)$ are the cluster weights, computed by requiring that the summation rules be exact for all shape functions ($n_h(\boldsymbol{l}_h) = \sum_{\boldsymbol{l}\in\mathcal{L}} \varphi_h(\boldsymbol{l}|\boldsymbol{l}_h)$). The calculation of the effective forces in eq. (7) is of complexity $\mathcal{O}(N_h N_c)$ where N_c is the number of lattice sites in a cluster of radius r_c. More details on the implementation of QC and an analysis of the accuracy and convergence of the method may be found in ref. [20]. The QC method has been successfully applied to a number of cases involving localized deformation and long-range fields, such as nanoindentation [25], nanovoid deformation [26, 27], and nanopillar compression [28].

2.2. The dynamical theory.

2.2.1. General framework. We start from the generalized Lagrange equation for *holonomic* non-conservative sytems, *i.e.* those where non-potential forces exist [29]:

$$\frac{d}{dt}\left(\frac{\partial L}{\partial \dot{\boldsymbol{q}}}\right) - \frac{\partial L}{\partial \boldsymbol{q}} = \boldsymbol{\mathcal{Q}}_p(\boldsymbol{q}, \dot{\boldsymbol{q}}, t) \tag{8}$$

where $L(\boldsymbol{q}, \dot{\boldsymbol{q}}, t) = T - U$ is the Lagrangian and $\boldsymbol{\mathcal{Q}}_p$ are the *generalized* non-potential forces. $T = \frac{1}{2}m\dot{\boldsymbol{q}}^T\dot{\boldsymbol{q}}$ and $U(\boldsymbol{q})$ are the kinetic and potential energies of the system, respectively[‡]. Without loss of generality, we assume that a linear relation exists between $\boldsymbol{\mathcal{Q}}_p$ and the velocities:

$$\boldsymbol{\mathcal{Q}}_p = -\boldsymbol{\Gamma}(\boldsymbol{q}, t)\dot{\boldsymbol{q}} \tag{9}$$

where $\boldsymbol{\Gamma}$ is a positive-definite matrix of dimension $(Nd \times Nd)$ whose components are the *damping* coefficients of the system. The symmetricity of $\boldsymbol{\Gamma}$ allows us to write expressions (9) as the derivatives $-\frac{\partial \mathcal{F}}{\partial \dot{\boldsymbol{q}}} = \boldsymbol{\mathcal{Q}}_p$ of the quadratic form [30]:

$$\mathcal{F} = \frac{1}{2}\dot{\boldsymbol{q}}^T\boldsymbol{\Gamma}\dot{\boldsymbol{q}} \tag{10}$$

which is ordinarily known as Rayleigh's dissipation function and represents the rate at which mechanical energy is converted to heat during a viscous process, $\dot{E} = -\dot{\boldsymbol{q}}^T\boldsymbol{\Gamma}\dot{\boldsymbol{q}}$. From eqs. (9) and (10), (8) now becomes:

$$\frac{d}{dt}\left(\frac{\partial L}{\partial \dot{\boldsymbol{q}}}\right) = \frac{\partial L}{\partial \boldsymbol{q}} - \frac{\partial \mathcal{F}}{\partial \dot{\boldsymbol{q}}} \tag{11}$$

which is Lagrange's equation for dissipative systems.

For homogeneous atomic systems, the viscosity matrix $\boldsymbol{\Gamma}$ can be written as:

$$\boldsymbol{\Gamma} = \nu\mathbf{I} \tag{12}$$

where ν is the velocity damping coefficient and $\mathbf{I}$ is the $(Nd \times Nd)$ identity matrix. It is often convenient to cast eq. (12) as $\boldsymbol{\Gamma} = m\tau^{-1}\mathbf{I}$ where m is an appropriate particle mass, and τ a characteristic damping time.

[‡] For simplicity, hereafter we omit the explicit dependence of L, T and U on time t.

2.2.2. Quasicontinuum reduction. Following the same notation as in Section 2.1, we now express eq. (11) in reduced QC coordinates. By recourse to expression (4), the system Lagrangian now becomes:

$$L(\boldsymbol{q},\dot{\boldsymbol{q}}) = \frac{1}{2}\sum_{\boldsymbol{l}} m(\boldsymbol{l}) \left[\sum_{\boldsymbol{l}_h\in\mathcal{L}_h} \dot{\boldsymbol{q}}_h(\boldsymbol{l}_h)\varphi(\boldsymbol{l}|\boldsymbol{l}_h)\right] \left[\sum_{\boldsymbol{l}'_h\in\mathcal{L}_h} \dot{\boldsymbol{q}}_h(\boldsymbol{l}'_h)\varphi(\boldsymbol{l}|\boldsymbol{l}'_h)\right] - \\ - U\left(\sum_{\boldsymbol{l}_h\in\mathcal{L}_h} \boldsymbol{q}_h(\boldsymbol{l}_h)\varphi(l|\boldsymbol{l}_h)\right) = L_h(\boldsymbol{q}_h,\dot{\boldsymbol{q}}_h) \quad (13)$$

Similarly, Rayleigh's dissipation function takes the form:

$$\mathcal{F}(\dot{\boldsymbol{q}}) = \frac{1}{2}\sum_{\boldsymbol{l}} m(\boldsymbol{l})\tau^{-1} \left[\sum_{\boldsymbol{l}_h\in\mathcal{L}_h} \dot{\boldsymbol{q}}_h(\boldsymbol{l}_h)\varphi(\boldsymbol{l}|\boldsymbol{l}_h)\right] \left[\sum_{\boldsymbol{l}'_h\in\mathcal{L}_h} \dot{\boldsymbol{q}}_h(\boldsymbol{l}'_h)\varphi(\boldsymbol{l}|\boldsymbol{l}'_h)\right] = \mathcal{F}_h(\dot{\boldsymbol{q}}_h) \quad (14)$$

Inserting eqs. (13) and (14) into eq. (11), the reduced problem becomes:

$$\sum_{\boldsymbol{l}} m(\boldsymbol{l})\varphi(\boldsymbol{l}|\boldsymbol{l}_h)\varphi(\boldsymbol{l}|\boldsymbol{l}'_h)\ddot{\boldsymbol{q}}_h(\boldsymbol{l}_h) = \\ \sum_{\boldsymbol{l}} \boldsymbol{f}(\boldsymbol{l}|\boldsymbol{q}_h)\varphi(\boldsymbol{l}|\boldsymbol{l}_h) - \sum_{\boldsymbol{l}} \tau^{-1} m(\boldsymbol{l})\varphi(\boldsymbol{l}|\boldsymbol{l}_h)\varphi(\boldsymbol{l}|\boldsymbol{l}'_h)\dot{\boldsymbol{q}}_h(\boldsymbol{l}_h) \quad (15)$$

where, as above, $\boldsymbol{f}(\boldsymbol{l}|\boldsymbol{q})$ is the value of $\boldsymbol{f}(\boldsymbol{q}) = U_{,\boldsymbol{q}}(\boldsymbol{q})$ at site $\boldsymbol{l}$[§]. The equation of motion in matrix notation becomes:

$$\boldsymbol{M}_h\ddot{\boldsymbol{q}}_h + \tau^{-1}\boldsymbol{M}_h\dot{\boldsymbol{q}}_h = \boldsymbol{f}_h(\boldsymbol{q}_h) \quad (16)$$

where

$$\boldsymbol{M}_h = \boldsymbol{M}(\boldsymbol{l}_h|\boldsymbol{l}'_h) = \sum_{\boldsymbol{l}} m(\boldsymbol{l})\varphi(\boldsymbol{l}|\boldsymbol{l}_h)\varphi(\boldsymbol{l}|\boldsymbol{l}'_h) \quad (17)$$

is the *consistent* mass matrix. By virtue of (12), eq. (16) is equivalent to:

$$\boldsymbol{M}_h\ddot{\boldsymbol{q}}_h + \boldsymbol{\Gamma}_h\dot{\boldsymbol{q}}_h = \boldsymbol{f}_h(\boldsymbol{q}_h) \quad (18)$$

In practice, the consistent mass matrix is commonly replaced by a lumped mass matrix for computational convenience. In QC we utilize the 'row-sum' lumping technique [31], by which the mass matrix diagonal entries are simply:

$$\boldsymbol{M}_h(\boldsymbol{l}_h,\boldsymbol{l}_h) = m_h(\boldsymbol{l}_h) = \sum_{\boldsymbol{l}} m(\boldsymbol{l})\varphi(\boldsymbol{l}|\boldsymbol{l}_h) \quad (19)$$

Eq. (19) now becomes the form for $\boldsymbol{M}_h$ used in eq. (16).

[§] Note that the definition of U at this stage need not coincide with that of the potential function Φ introduced in Section 2.1.

Equation (16) is an inhomogeneous second-order ODE (ordinary differential equation) representing viscous damping dynamics. The homogeneous form of this class of equations can be expressed as a matrix ODE of the form:

$$\dot{\boldsymbol{x}} = -\tau^{-1}\mathbf{I}\boldsymbol{x} = \boldsymbol{A}\boldsymbol{x}$$

which admits characteristic solutions of the type $\boldsymbol{x} = \boldsymbol{x}_0 \exp\{\boldsymbol{A}t\}$, where $\boldsymbol{x} = \{\boldsymbol{q}, \dot{\boldsymbol{q}}\}$ is a $2Nd$-dimensional variable that represents a point in phase space, and $\boldsymbol{x}_0 = \{\boldsymbol{q}_0, \dot{\boldsymbol{q}}_0\}$ is the initial state of the crystal. The system (block) matrix is:

$$\boldsymbol{A} = \begin{bmatrix} 0 & 1 \\ 0 & -\tau^{-1} \end{bmatrix}$$

However, since the generalized potential U is not a simple function of $\boldsymbol{q}$ or t, particular solutions for eq. (16) are not available *a priori*. Next, we make the following assumption: we regard the reduced set of representative atoms $\mathcal{T}_h$ as an ensemble of nodes suspended in a *medium* or solvent representing the neglected degrees of freedom. The effect of this medium may be approximated by a frictional drag on the $\{\boldsymbol{q}_h\}$ set as well as random fluctuations associated with the thermal motions of the solvent particles. This behavior, known as Langevin dynamics, is best described using stochastic differential equations to account for the omitted DOF [32]. In adapting eq. (16) to a Langevin equation, we must bear in mind that in the general case of unstructured triangulations $\boldsymbol{M}_h$ and $\boldsymbol{f}_h$ are also spatially-varying fields and the parameters that govern the dynamic behavior, notably τ (or ν), will also in general be spatial fields, $\tau_h = \tau(\boldsymbol{q}_h)$.

To map eq. (16) to a Langevin equation, we perform the following decomposition on $\boldsymbol{f}(\boldsymbol{l}|\boldsymbol{q})$ (first term of the r.h.s. of eq. (15)):

$$\boldsymbol{f}(\boldsymbol{l}|\boldsymbol{q}) = \boldsymbol{f}_b(\boldsymbol{l}|\boldsymbol{q}) + \boldsymbol{R}(\boldsymbol{l}, t) \tag{20}$$

where $\boldsymbol{f}_b$ are the body forces, defined as in Section 2.1, eq. (6), and $\boldsymbol{R}(\boldsymbol{l}, t)$ is an instantaneous random force. Eq. (20) implies that U has the meaning of a potential of *mean force* [33], *i.e.* $U(\boldsymbol{q}) \equiv E(\boldsymbol{q}) + \int_X \boldsymbol{R}(\boldsymbol{q}, t) d\boldsymbol{q}$. After the above additive decomposition, the generalized equation of motion becomes:

$$\boldsymbol{M}_h\ddot{\boldsymbol{q}}_h + \tau^{-1}\boldsymbol{M}_h\dot{\boldsymbol{q}}_h = \boldsymbol{f}_b(\boldsymbol{q}_h) + \boldsymbol{R}_h(t) \tag{21}$$

where, for consistency:

$$\boldsymbol{R}_h(t) = \boldsymbol{R}(\boldsymbol{l}_h, t) = \sum_{\boldsymbol{l}} \boldsymbol{R}(\boldsymbol{l}, t)\varphi(\boldsymbol{l}|\boldsymbol{l}_h) \tag{22}$$

When τ is much larger than the relaxation time scale associated with the fluctuations of the random force, equation (21) is the ordinary Langevin equation of a so-called *Markovian* system. Under such approximation $\boldsymbol{R}(\boldsymbol{l}, t)$ can be taken as a stationary Gaussian random variable whose first and second moments are:

$$\begin{array}{l} \langle \boldsymbol{R}(\boldsymbol{l}, t) \rangle = 0 \\ \langle \boldsymbol{R}(\boldsymbol{l}, t) \otimes \boldsymbol{R}(\boldsymbol{l}, t') \rangle = 2\nu k_B T \; \mathbf{I} \; \delta(t - t') \end{array} \tag{23}$$

where the first expression refers to the time average of the random force and the second gives the covariance matrix. Here k_B and T are, respectively, Boltzmann's constant and the absolute temperature, and $\delta(t)$ is Dirac's delta function. According to this definition, the random force represents a Wiener process with zero expected value and quadratic variation on $[0,t]$ equal to $t-t'$, $\forall\ t' \in [0,t]$ [34]. In relation to Langevin dynamics, the definition of the covariance matrix stems from the imposition of correct equilibrium averages, and implies that $\boldsymbol{R}_h(t)$ has no self-correlation, *i.e.* the system satisfies the dissipation-fluctuation theorem [35].

Langevin dynamics can also be used as a thermostat, adding the dissipative forces and the random fluctuations to the Hamiltonian dynamics to allow molecular dynamics simulations to explore a canonical ensemble. As we shall see, we solve eq. (21) at the nodal level, with each representative atom being immersed in a homogeneous medium connected to a thermal bath represented by $\boldsymbol{R}_h(t)$. The temperature of the system being simulated is maintained via the relationship between $\boldsymbol{R}_h(t)$ and ν (eq. (23)). In Section 3 we discuss the details and numerical aspects of the implementation, and the implications of the configurational space reduction ($\mathcal{L} \rightarrow \mathcal{L}_h$).

2.3. Time-stepping algorithms.

In calculations, we shall envision a time-stepping process by which a dynamic trajectory is approximated at times $t_0, ...t_n, t_{n+1} = t_n + \Delta t, ...$ First, we recast eq. (16) as the following initial value problem:

$$\dot{\boldsymbol{x}} = F(\boldsymbol{x}), \quad \boldsymbol{x}(0) = \boldsymbol{x}_0 \tag{24}$$

where $\boldsymbol{x}$ and $\boldsymbol{x}_0$ have the same meaning as in the preceding section, and F is a *Lipschitz* map. We shall denote by $\boldsymbol{x}_n$ the numerical solution at time t_n. We define as algorithm a mapping $\boldsymbol{S}(\Delta t) : X \rightarrow X$ such that:

$$\boldsymbol{S}(\Delta t = 0^+) = id, \quad \left[\frac{d}{d(\Delta t)}\boldsymbol{S}(\Delta t)\boldsymbol{x}\right]_{\Delta t = 0^+} = F(\boldsymbol{x}), \quad \forall \boldsymbol{x} \in X \tag{25}$$

$\boldsymbol{S}(\Delta t)$ is applied recursively to compute the numerical solution as $\boldsymbol{x}_n = \boldsymbol{S}^n(\Delta t)\boldsymbol{x}_0$. The algorithm must be convergent in the sense that, if $\boldsymbol{x}(t)$ is the exact trajectory, then:

$$\lim_{n\rightarrow\infty} \boldsymbol{S}(t/n)\boldsymbol{x}_0 = \boldsymbol{x}(t) \tag{26}$$

We are interested in stable and accurate time propagators for stochastic dynamics. In mechanical terms, long-time stability follows from the symplectic nature of the time propagator [36]. In statistical terms, symplecticity implies exact conservation of magnitudes in phase space, *i.e.* applying Gibbs statistical mechanics to well-defined ensembles of physical states [37].

3. Numerical implementation.

3.1. Time integration algorithm.

The most widely used class of direct time integration methods for solving problem (24) (or, equivalently, eq. (16)) is the Newmark family of methods [38]. The general form of the Newmark algorithm for a mechanical system with external forces $\boldsymbol{F}$ is [31]:

$$\boldsymbol{M}\boldsymbol{a}_{n+1} + \boldsymbol{C}\boldsymbol{v}_{n+1} + \boldsymbol{K}\boldsymbol{d}_{n+1} = \boldsymbol{F}_{n+1} \tag{27a}$$

$$\boldsymbol{d}_{n+1} = \boldsymbol{d}_n + \Delta t\boldsymbol{v}_n + \frac{\Delta t^2}{2}\left[(1-2\beta)\boldsymbol{a}_n + 2\beta\boldsymbol{a}_{n+1}\right] \tag{27b}$$

$$\boldsymbol{v}_{n+1} = \boldsymbol{v}_n + \Delta t\left[(1-\gamma)\boldsymbol{a}_n + \gamma\boldsymbol{a}_{n+1}\right] \tag{27c}$$

where $\boldsymbol{d}_n$, $\boldsymbol{v}_n$ and $\boldsymbol{a}_n$ are the approximations of $\boldsymbol{q}(t_n)$, $\dot{\boldsymbol{q}}(t_n)$ and $\ddot{\boldsymbol{q}}(t_n)$, respectively. Eq. (27a) is the equation of motion in terms of the approximate solution, and (27b) and (27c) are finite difference approximations of the velocity and displacement vectors. The parameters β and γ dictate the stability and accuracy of the algorithm and contain as special cases many well-known and widely-used integration algorithms [31]. We now discuss our algorithm parametrization. For linear problems with diagonal $\boldsymbol{M}$ and $\boldsymbol{C}$ matrices, it is convenient to set $\beta = 0$ for *explicit* dynamics. This is advantageous as all matrices are trivially invertible and no matrix solver is needed. Explicit methods, however, only admit values of $\gamma \geqslant \frac{1}{2}$, which give only conditionally stable phase-space trajectories. The stability limit when $\beta = 0$ is achieved by imposing $\gamma = \frac{1}{2}$ whereupon we recover the well-known central differences algorithm. This ($\beta = 0$; $\gamma = \frac{1}{2}$) version of the Newmark method is second-order accurate and is known to be symplectic and momentum preserving [39, 40]. However, the simplicity furnished by this choice of parameters sets limitations on the affordable time scale achievable in simulations. Generally, the critical time step securing the stability of the central difference method for a linear undamped system is given by the Courant condition [41], governed in QC by the shortest separation between representative atoms. In the atomistic limit of the method, this can lead to slow temporal evolutions. Alternative implicit integration techniques for long time step Langevin molecular dynamics simulations have been developed, see, *e.g.*, refs. [42] and [43]. Time-saving and multiple-time-step algorithms have also been proposed for Langevin dynamics [44, 37]. Helfand and co-workers have proposed integrators for generalized stochastic differential equations [45, 46].

By construction, $\boldsymbol{M} \equiv \boldsymbol{M}_h$ and $\boldsymbol{C} \equiv \boldsymbol{\Gamma}_h$ are diagonal matrices in our QC-Langevin framework (note that here, by direct mapping to eq. (16), $\boldsymbol{K} \equiv \boldsymbol{K}_h = 0$). Each one of the entries in the diagonal of $\boldsymbol{M}_h$ in eqs. (16) and (21) corresponds to the nodal masses m_h. By virtue of definition (19), $m_h = m(\boldsymbol{l})n_h(\boldsymbol{l}_h)$, where $n_h(\boldsymbol{l}_h)$ is the nodal weight, defined as in Section 2.1. In fully resolved systems like those QC is concerned with, $m(\boldsymbol{l}) = m_a$, $\forall\ \boldsymbol{l}, t$, where m_a is the atomic mass. Similarly, the diagonal components of $\boldsymbol{\Gamma}_h$ are $\nu_h = m_h/\tau$, where τ is also assumed to be constant in time. This linearity in the formulation allows eq. (21) to be transformed from a matrix equation into a set of individual equations for each degree of freedom. We can then rearrange eqs. (27) into a predictor step:

$$d_{n+1} = d_n + \Delta t v_n + \frac{\Delta t^2}{2} a_n \tag{28}$$

and a corrector one:

$$a_{n+1} = \frac{f_{h_{n+1}} - c_h \left(v_n + \frac{\Delta t}{2} a_n\right)}{m_h + c_h \frac{\Delta t}{2}} \tag{29a}$$

$$v_{n+1} = v_n + \frac{\Delta t}{2} \left(a_n + a_{n+1}\right) \tag{29b}$$

where, from eq. (20), $f_h = f_{b_h} + R_h$ is the nodal force consisting of the internal body forces and the random force.

3.2. Random force.

Instantaneous values of R_h are generated by sampling from a normal distribution using the Box-Muller transformation [47], *i.e.* if u_1 and u_2 are independent random variables that are uniformly distributed in the interval $(0, 1]$ then:

$$z_1 = (-2 \ln u_1)^{\frac{1}{2}} \cos(2\pi u_2)$$

and

$$z_2 = (-2 \ln u_1)^{\frac{1}{2}} \sin(2\pi u_2)$$

are independent, normally-distributed variables with zero mean and unit variance. We discard one of these values at random and trivially convert the other to a normal distribution of mean μ and variance σ^2 as $r = \mu + \sigma z$, where, after (23), $\mu = 0$ an $\sigma^2 = 2m\tau^{-1}k_B T/\Delta t$. This value of $R_h = r$ is then added to the body force f_{b_h} that enters eq. (29a) as f_h.

3.3. Numerical tests and determination of the timestep.

The stability criterion for the ($\beta = 0$; $\gamma = \frac{1}{2}$) Newmark integrator is set by the shortest separation between adjacent representative atoms. The most stringent case is of course that of atomistic resolution, in which case Δt is conventionally set to values smaller than the fastest characteristic eigenfrequency $\omega_{\max} = 2\pi f_{\max}$ of the system. However, conditionality is removed from the stability definition by ensuring that $\Delta t < \tau$ [48]. Therefore, the locus of stable $(\Delta t, \tau)$ diads is a triangle in the positive quadrant of the Δt-τ plane, delimited by the two stability conditions $\Delta t < 1/f_{\max}$ and $\Delta t < \tau$. Figure 1 schematically shows the stability region in the Δt-τ space. However, the specific choice of the time step and the damping time within this region is material and problem dependent, and remains somewhat *ad hoc* so that numerical tests must be carried out to establish the optimal choice. These tests have been performed in the high-frequency limit, *i.e.* for atomistic systems in the canonical ensemble, seeking the highest possible Δt for which energy is conserved.

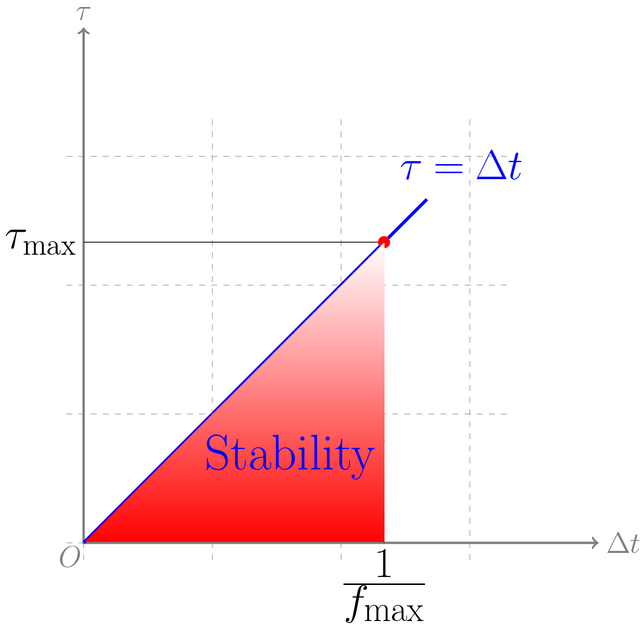

Figure 1. Schematic representation of the Δt-τ stability space for Langevin dynamics. The value $\nu_{\rm min} = m_a/\tau_{\rm max}$ gives the minimum viscosity that can be used in simulations.

After an extensive number of numerical tests, the selected values of Δt and τ that produce stable trajectories while maximizing time advancement are given in Table 1 for the two materials studied here. The corresponding values of the inverse of $f_{\rm max}$ are also given for reference. By way of comparison, Qu *et al* use a maximum damping coefficient of approximately one half the Debye frequency [18], which is $\approx$ 8.92 THz for Al and $\approx$ 5.01 THz for Ta [49].

Table 1. Time step, characteristic damping time, maximum eigenfrequency $f_{\rm max} = \omega_{\rm max}/2\pi$ of a perfect atomic crystal for the two materials considered in this work, namely Al and Ta.

Material	Δt (fs)	τ (fs)	$1/f_{\rm max}$ (fs)
Al	5.29	70.55	106.0
Ta	0.66	8.82	184.8

3.4. The harmonic approximation in the QC framework.

For the present analysis, let us recover momentarily the notation introduced in Section 2.1. We start with the harmonic form of the potential function $\Phi(\boldsymbol{q}_h)$:

$$\Phi(\boldsymbol{q}_h) = \frac{1}{2}\left(\boldsymbol{q}_h - \boldsymbol{q}_0\right)\boldsymbol{K}(\boldsymbol{q}_0)\left(\boldsymbol{q}_h - \boldsymbol{q}_0\right)^T \qquad (30)$$

where $\boldsymbol{q}_0$ is a Nd vector representing an equilibrium configuration of the system and $\boldsymbol{K}$ is the *Hessian* of $\Phi(\boldsymbol{q}_h)$. Without loss of generality, let us assume that $\boldsymbol{q}_0$ represents the *undeformed* or reference configuration in $\mathcal{L}_h$, *i.e.* a particular solution of eq. (5) that satisfies the equilibrium conditions (6) when $\Phi^{\text{ext}} = 0$. Then, the components of $\boldsymbol{K}$ (also known as the *force constants*) are:

$$K_{\alpha\beta}(\boldsymbol{l}_h, \boldsymbol{l}'_h) = \frac{\partial^2 E}{\partial q_\alpha(\boldsymbol{l}_h)\partial q_\beta(\boldsymbol{l}'_h)} \quad \alpha, \beta = 1, ..., d$$

For simplicity, we hereafter restrict this study to a three-dimensional system occupying a volume V in an *Euclidean* space and fix $d = 3$. Let us remark at this point that the Hessian of the harmonic energy landscape is also mesh and cluster size dependent.

The equations of motion for the reduced QC system interacting via a harmonic potential of the form given in (30) are:

$$\boldsymbol{M}_h \ddot{\boldsymbol{q}}_h = \boldsymbol{K}\left(\boldsymbol{q}_h - \boldsymbol{q}_0\right) \tag{31}$$

We now define the *mass-weighted displacement* as:

$$\boldsymbol{u} = \sqrt{\boldsymbol{M}_h}\left(\boldsymbol{q} - \boldsymbol{q}_0\right) \tag{32}$$

and perform the following change of variable:

$$\boldsymbol{K} = \sqrt{\boldsymbol{M}_h}\ \boldsymbol{D}\ \sqrt{\boldsymbol{M}_h} \tag{33}$$

Then, the harmonic potential and the equations of motion become, respectively:

$$\Phi(\boldsymbol{u}_h) = \frac{1}{2}\boldsymbol{u}_h \boldsymbol{D} \boldsymbol{u}_h^T \tag{34}$$

$$\ddot{\boldsymbol{u}}_h = \boldsymbol{D}\boldsymbol{u}_h \tag{35}$$

where $\boldsymbol{D}$ is the $(3N_h \times 3N_h)$ *dynamical* matrix. In general, $\boldsymbol{D}$ is Hermitian, and by virtue of the geometric symmetries of cubic metals it is real as well, and hence symmetric. For eq. (35) we seek solutions of the type [50]:

$$\boldsymbol{u}_h(\boldsymbol{q}_h) = \boldsymbol{\epsilon}_h \exp\left[-i\left(\omega t - \boldsymbol{k}\boldsymbol{q}_h\right)\right] \tag{36}$$

where $\boldsymbol{\epsilon}_h$ is a polarization direction, ω is a vibration frequency, and $\boldsymbol{k}$ is a wave vector. With this form, eq. (35) becomes:

$$\boldsymbol{\epsilon}_h\ \omega^2 = \boldsymbol{D}\boldsymbol{\epsilon}_h \tag{37}$$

Solving this eigenvalue problem[‖] yields the $3N_h$ independent normal modes of vibration ω and eigenvectors $\boldsymbol{\epsilon}_h$ of the reduced QC system.

[‖] Since $\boldsymbol{D}$ is real and symmetric, it can always be diagonalized by an orthogonal matrix $\boldsymbol{\epsilon}$.

Now, from definition (33), the components of the dynamical matrix are:

$$D_{\alpha\beta}(\boldsymbol{l}_h, \boldsymbol{l}'_h) = \frac{K_{\alpha\beta}(\boldsymbol{l}_h, \boldsymbol{l}'_h)}{\sqrt{m(\boldsymbol{l}_h)m(\boldsymbol{l}'_h)}} \tag{38}$$

where the force constant $K_{\alpha\beta}(\boldsymbol{l}_h, \boldsymbol{l}'_h)$ gives the reaction along β of node $\boldsymbol{l}'_h$ when node $\boldsymbol{l}_h$ is infinitesimaly displaced along α. Recovering the definition of the nodal mass from Section 3.1, $m(\boldsymbol{l}_h) = m_a n_h(\boldsymbol{l}_h)$, we can re-write eq. (38) as:

$$D_{\alpha\beta}(\boldsymbol{l}_h, \boldsymbol{l}'_h) = \frac{K_{\alpha\beta}(\boldsymbol{l}_h, \boldsymbol{l}'_h)}{m_a\sqrt{n_h(\boldsymbol{l}_h)n_h(\boldsymbol{l}'_h)}} \tag{39}$$

In the atomistic limit, all the nodal weights are equal to unity and eq. (39) takes the standard microscopic form [50]. Next, we make use of the expressions derived by Knap and Ortiz [20] to define the nodal weights in the context of cluster-based summation rules for QC¶:

$$n_h(\boldsymbol{l}_h) = \frac{\sum_{\boldsymbol{l}\in\mathcal{L}} \ \varphi_h(\boldsymbol{l}|\boldsymbol{l}_h)}{\sum_{\boldsymbol{l}'_h\in\mathcal{L}_h}\sum_{\boldsymbol{l}\in\mathcal{C}_h(\boldsymbol{l}'_h)} \ \varphi_h(\boldsymbol{l}|\boldsymbol{l}_h)} \tag{40}$$

The numerator in eq. (40) simply sums to the total number of atoms in the system, N. For its part, the double sum in the denominator can be approximated for structured meshes (all simplices in $\mathcal{T}_h$ equal) as N_cN_h:

$$n_h(\boldsymbol{l}_h) \equiv n_h \approx \frac{N}{N_cN_h}$$

When $N_cN_h > N$, signaling cluster overlap, then n_h is set equal to one. This simplified form of n_h is then introduced in eq. (39), which then becomes:

$$D_{\alpha\beta}(\boldsymbol{l}_h, \boldsymbol{l}'_h) \approx \frac{N_cN_h}{m_aN}K_{\alpha\beta}(\boldsymbol{l}_h, \boldsymbol{l}'_h) \tag{41}$$

The number of atoms N_c in a cluster of radius r_c is $N_c = \frac{4\pi}{3}{r_c}^3\rho_a$, where $\rho_a = N/V$ is the atomic density of the undeformed configuration. Similarly, the ratio N/N_h gives the number of atoms in each simplex of a structured mesh. Assuming tetrahedral triangulations with a characteristic element size h:

$$\frac{N}{N_h} \approx \rho_a c h^3$$

where c is geometric constant ($c = \frac{1}{\sqrt{72}}$ for regular tetrahedra). It then follows from eq. (41) that:

$$D_{\alpha\beta}(\boldsymbol{l}_h, \boldsymbol{l}'_h) \approx \frac{4\pi}{3m_ac}\left(\frac{r_c}{h}\right)^3 K_{\alpha\beta}(\boldsymbol{l}_h, \boldsymbol{l}'_h) \tag{42}$$

Noting that $\omega \propto \sqrt{D}$ and lumping the prefactor on the r.h.s. of eq. (42) into a single constant C, we have that:

$$\omega \propto C\left(\frac{r_c}{h}\right)^{\frac{3}{2}}\sqrt{K_{\alpha\beta}(\boldsymbol{l}_h, \boldsymbol{l}'_h)} \tag{43}$$

¶ In Section 3.2 of their paper.

In fcc crystals, symmetry reduces the number of force constants for the undeformed configuration to three independent values for the first nearest neighbor shell, and two for the second [51, 52]. These force constants possess non-obvious system-size dependences themselves, although, generally, softening is to be expected with increasing interparticle distance.

Eq. (43) contains length scale dependencies of fundamental importance in the Quasicontinuum context, and effectively establish the 'hardness' of the vibrational frequency spectrum in a QC system. The *mass* factor $(r_c/h)^{3/2}$ suggests that coarser meshes give rise to softer spectra, whereas larger clusters produce higher energy vibrations. The dependence on mesh and cluster size of the other term in eq. (43) —the force constants— will be explored in Section 4.1.3.

3.5. Thermal expansion within the quasiharmonic approximation.

To link the vibrational properties of a QC system with a fundamental crystal property such as thermal expansion, we start from the reduced system introduced in Sections 2.1 and 2.2.2. From eq. (13), suppose that the system is governed by a Hamiltonian of the form:

$$H_h(\boldsymbol{q}_h, \boldsymbol{p}_h, \theta) = \sum_{\boldsymbol{l}_h} \frac{\boldsymbol{p}_h^{\,2}}{2m_h} + \Phi_h(\boldsymbol{q}_h, \theta) \tag{44}$$

where $\boldsymbol{p}_h = m_h \dot{\boldsymbol{q}}_h$ are the momenta. Further, in eq. (44) we assume isotropic thermal expansion (*e.g.* cubic crystals) whence only a dependence on the volumetric strain $\theta = \Delta V/V$ need be considered. The partition function for the system of *distinguishable* particles associated with this Hamiltonian is [53]:

$$Z_h(\theta, T) = \frac{1}{(2\pi\hbar)^{3N_h}} \int \exp\Big\{ - \frac{H_h(\boldsymbol{q}_h, \boldsymbol{p}_h, \theta)}{k_B T} \Big\} d\boldsymbol{q}_h d\boldsymbol{p}_h \tag{45}$$

where $\hbar$ is Planck's constant. Assuming the harmonic form of eq. (34) for Φ_h, the free energy takes the form:

$$F_h(\theta, T) \approx \Phi_h(\boldsymbol{0}, \theta)) - k_B T \left(\frac{3N_h}{2} \ln \left\{ \frac{m_h {k_B}^2 T^2}{\hbar^2} \right\} - \sum_i^{3N_h} \ln \left\{ \omega_i(\theta) \right\} \right) \tag{46}$$

where, again, the $\omega_i(\theta)$ are the eigenfrequencies of $K_{\alpha\beta}(\boldsymbol{l}_h, \boldsymbol{l}'_h)|_{\boldsymbol{0}}$, which, by virtue of the quasiharmonic approximation, are assumed to depend on θ rather than T. The full derivation of the free energy expression in eq. (46) is given in the Appendix.

Now, in the limit of small deformations, the volumetric expansion coefficient β for isotropic media is given by the following thermodynamic relation:

$$\beta = 3\alpha = \frac{1}{(1-\theta)^2} \left(\frac{\partial \theta}{\partial T} \right)_P = \frac{1}{(1-\theta)^2} \left(\frac{\partial \theta}{\partial P} \right)_T \left(\frac{\partial P}{\partial T} \right)_V =$$

$$= -\frac{1}{B(1-\theta)} \left(\frac{\partial P}{\partial T} \right)_V \tag{47}$$

where α, P and B are, respectively, the linear expansion coefficient, the pressure and the isothermal bulk modulus. The term $(1-\theta)^{-1}$ is simply the ratio V/V_0, where V_0 is a reference volume usually taken as that of the undeformed configuration at 0K . The pressure can be directly obtained as

$$P = -\left(\frac{\partial F}{\partial V}\right)_T = \frac{1}{V}\frac{\partial F}{\partial\{\ln(1-\theta)\}}$$

and therefore:

$$\alpha = -\frac{1}{3BV_0}\frac{\partial^2 F}{\partial T\partial\{\ln(1-\theta)\}} \tag{48}$$

Inserting eq. (46) into (48), the *reduced* thermal expansion coefficient evaluates to:

$$\alpha = -\frac{k_B}{3BV_0}\sum_{i=1}^{3N_h}\frac{\partial\{\ln\omega_i(\theta)\}}{\partial\{\ln(1-\theta)\}} \tag{49}$$

where the term inside the sum is customarily known as the *individual Grüneisen* parameter of each normal mode and measures the variation of ω_i with deformation [54, 55]. Thus, within the quasiharmonic approximation, it is assumed that the Grüneisen parameter(s) is(are) independent of temperature, which gives rise to constant thermal expansion coefficients in the entire temperature range [56]. This is generally acceptable for transition metals, although notable exceptions exist, as we shall see. See Touloukian *et al* [60], Srivastava [56] and Ho and Taylor [57] for a more in-depth discussion on the validity of the quasiharmonic approximation for thermal expansion calculations.

The last two terms on the r.h.s. of eq. (46) give an idea of the loss of entropy attendant to the reduced QC system. Limiting the sums at N_h particles, rather than N, will intrinsically result in lower entropic contributions to the total free energy. In addition to reduced numbers of available eigenstates, equation (43) shows that these are modulated by the *weight factor* $(r_c/h)^{3/2}$ (which typically < 1), *i.e.*, for a fixed N_h, the entropic contribution of the reduced set of frequencies will be further diminished by mesh effects. Both of these effects impact directly the thermal expansion coefficient of the material by way of equation (49).

In calculations, we compute the free energy as in eq. (46) and obtain α directly from eq. (49). The term $\Phi_h(\mathbf{0},\theta)$ and the eigenfrequencies are obtained statically with QC as a function of θ. The dynamical matrix coefficients (38) can be evaluated from a purely elastic continuum framework [58] or using Richardson's interpolation to evaluate the force constants [59]. The thermal expansion coefficients computed in this fashion are then compared with the *dynamic* values of α.

Next, we present results of thermal expansion measurements from 3D dynamic QC simulations in two representative materials, namely Al and Ta. Subsequently, analyses of the measured data are provided within the quasiharmonic approximation framework derived in this Section.

4. Results

In this section, we study the dynamic behavior of Al and Ta as a function of the three critical QC parameters: system size, N, mesh size, N_h, and cluster size, r_c. The objective is to ascertain the effect of each of these on the temperature-dependent thermal expansion of both material systems. To measure α directly from canonical QC runs (*i.e.* in the N_hPT ensemble), we perform a series of simulations for a given configuration (N, N_h, r_c) at several temperatures using the parametrization extracted in Section 3.3. When the system is seen to reach steady state, we perform a time average of the observed volume as:

$$\langle V\rangle_T = \frac{\int_{t_1}^{\infty} V_i(t)|_T \, dt}{\int_{t_1}^{\infty} dt} = {n_t}^{-1}\sum_{i=1}^{n_t} V_i(N, N_h, r_c)|_T \tag{50}$$

where n_t is a sufficiently high number of time steps and V_i is the instantaneous system volume at time $t_i = i\Delta t$. Here, $i = 1$ marks the first time step after steady state has been achieved. V_i is computed directly from the addition of all the tetrahedral element volumes in $\mathcal{T}_h$. Then, the thermal expansion coefficient is straightforwardly obtained as:

$$\alpha(N, N_h, r_c) = \frac{1}{3V_0}\frac{d\left\{\langle V\rangle(T)\right\}}{dT} \tag{51}$$

where $V_0(N, N_h, r_c)$ is the equilibrium volume of the system as obtained via static relaxation. As is customary [60, 61], the thermal expansion coefficient is evaluated at room temperature (298K) from a third-degree polynomial fit to the data.

For simplicity, hereafter we refer to cluster sizes in terms of the maximum nearest-neighbor shell they encompass. Thus, by recursive neighbor shell construction in the fcc lattice, cluster sizes of 2, 3 and 4 in reality indicate $r_c \approx a_0$, $1.225a_0$, and $1.414a_0$, which contain 18, 42 and 54 lattice points respectively$^+$. For a number of reasons not related to this paper [20], our test samples are always finite cubic systems. This introduces the need to monitor surface effects and capillary forces —nonexistant in periodic systems— on volume expansion, although these are not expected to be important for sufficiently large systems.

4.1. Aluminum results.

4.1.1. Thermal expansion from dynamic simulations. Fcc Al is modeled using the glue potential developed by Ercolessi and Adams [63], which is fitted, among other parameters, to the experimental lattice constant of $a_0 = 4.032$ Å and the three cubic elastic moduli. One salient feature of this potential is that it possesses excellent surface and thermal properties (see also: Liu *et al* [64]), something of particular importance in our case, where only finite systems limited by surfaces, upon which boundary conditions are applied, are simulated.

$^+$ Face-centered cubic lattice shells can be constructed by recourse to the formula [62]: $d_{\rm shell} = \sqrt{\frac{i_{\rm shell}}{2}}$, where $d_{\rm shell}$ and $i_{\rm shell}$ are the distance (in lattice units) and index number of each nearest-neighbor shell.

QC can be thought of as a technique that contains full atomistics and continuum elasticity as special limits. As such, the natural limit of our finite-temperature QC at the finest scale is MD. Ercolessi and Adams give a thermal expansion coefficient of $\alpha_{\mathrm{MD}} = 1.79 \times 10^{-5}$ K^{-1} at room temperature for a periodic Al system containing 10752 particles [63]*. To establish our atomistic baseline we first perform dynamic QC simulations at zero pressure of finite $16a_0 \times 16a_0 \times 16a_0$ and $32a_0 \times 32a_0 \times 32a_0$ Al crystals containing, respectively, 17969 and 137313 atoms. V_0 for these systems is 2.662×10^5 and 2.138×10^6 Å^3, respectively. Figure 2 shows the temperature dependence of the systems' volume. Third-degree polynomial fits to the data yield $\alpha_{\mathrm{at}} = 1.72 \times 10^{-5}$ and 1.70×10^{-5} K^{-1} at 298K for the 17969 and 137313-atom systems respectively. The polynomial coefficents are given in Table 2. The small discrepancy ($\approx 4\%$) between the periodic MD sample considered by Ercolessi and Adams and our finite systems adds confidence to the QC calculation and suggests that the associated surface effects are small.

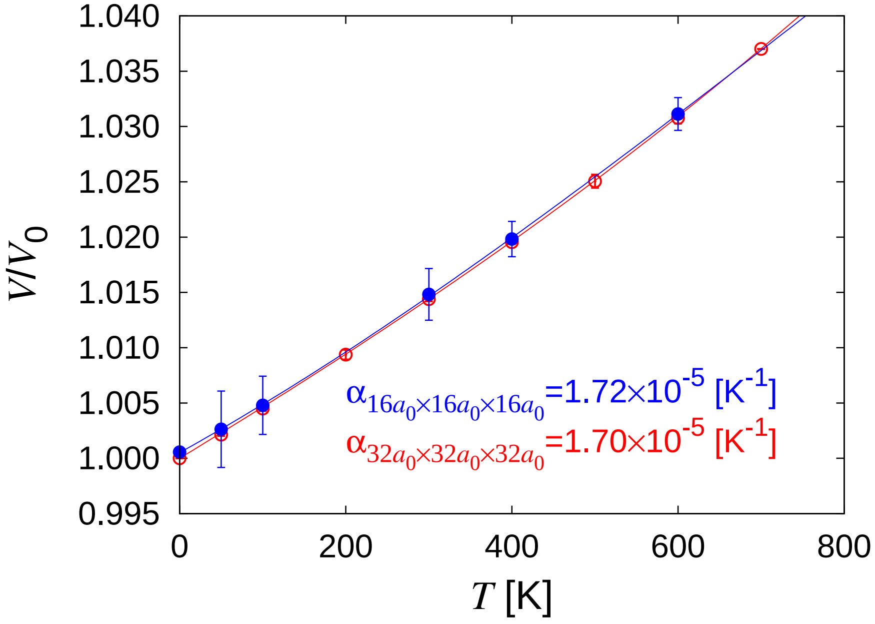

Figure 2. Thermal expansion behavior of two finite Al crystals containing 17969 (dimensions: $16_0 \times 16_0 \times 16a_0$) and 137313 ($32a_0 \times 32a_0 \times 32a_0$) atoms. The values at 298K of third-degree polynomial fits give thermal expansion coefficients of $\alpha = 1.72 \times 10^{-5}$ and 1.70×10^{-5} K^{-1} respectively. The error bars (very small for the $32_0 \times 32_0 \times 32a_0$ system) are associated with volume fluctuations in equilibrium.

Next we study cluster and mesh size effects on the values of V_0 in eq. (51) for both sample sizes considered. This is important because errors in the computation of α from eq. (51) can also enter via the calculation of V_0. For this analysis, we conveniently express the mesh size in terms of the total number of represented atoms $n'_h = N/N_h$,

---

* Pearson gives an experimental value of 2.36×10^{-5} K^{-1} [65].

Table 2. Coefficients of the third degree polynomials $V(T)/V_0 = aT^3 + bT^2 + cT + d$ plotted in Fig. 2. From eq. (51), $\alpha(T) = \frac{1}{3}\left(3aT^2 + 2bT + c\right)$. d is always necessarily equal to one, as, at $T = 0$, $V(0) = V_0$ is imposed.

Sample size	a	b	c	d
$16a_0 \times 16a_0 \times 16a_0$	-8.53×10^{-12}	2.06×10^{-8}	4.17×10^{-5}	1.00
$32a_0 \times 32a_0 \times 32a_0$	6.10×10^{-12}	6.18×10^{-9}	4.56×10^{-5}	1.00

which can be regarded as a first-order measure of the nodal weight. In this fashion, the inverse of n_h' acts as the N-normalized number of representative atoms. By way of example, Fig. 3 shows different degrees of mesh coarsening for the $32a_0 \times 32a_0 \times 32a_0$ Al crystals. Two types of meshes have been generated, namely, simple cubic (sc) and face-centered cubic (fcc)[♯]. The variation of V_0 as a function of $1/n_h'$ and r_c is displayed in Fig. 4. Results are normalized to the fully-atomistic relaxed volumes given in the previous paragraph. For small numbers of N_h, both parameters have a noticeable influence on the value of V_0. However, at $1/n_h' \approx 0.14$, V_0 is already fully converged to the relaxed atomistic equilibrium volumes.

To ascertain the effect of mesh and cluster sizes on the value of the thermal expansion coefficient in the $32a_0 \times 32a_0 \times 32a_0$ system, we have carried out simulations with six different degrees of coarseness for cluster sizes of 2, 3 and 4. By way of example, in Fig. 5 we show the volume vs. time curves as a function of temperatures for the (N=137313, N_h=729, r_c=4) system. $\langle V\rangle(T)$ is measured during $\sim$30 to 50 ps according to eq. (50) after steady state is reached. All simulations are always preceded by a 25-ps thermalization period from an initial state corresponding to the 'frozen' (zero kinetic energy), unrelaxed cubic sample (2.138×10^6 Å^3). All the cases simulated here are qualitatively similar to that shown in Fig. 5, with larger fluctuations occurring for a given temperature as N_h decreases.

Results for four representative configurations are shown in Fig. 7. In this case, using third-degree polynomial fits is inadequate because the structure displayed by each curve (each mesh) is not necessarily related to the V-T behavior. This structure, however, would be artificially captured by the polynomial fits, resulting in spurious thermal expansion coefficients. Hence, for this specific analysis we assume constant thermal expansion and simply fit the data to a linear equation of the form:

$$V_{\text{eq}}(T) = cT + V_0 \tag{52}$$

where, naturally, $\alpha = c/3V_0$. Results for α for all the cases considered are compiled in Table 3. In light of the results, two general assertions can be made. First, the dominant linear behavior of the V-T relation is gradually lost as h grows. Indeed, for the 729-node case, the system's volume shows no clear temperature dependence and only uncorrelated

---

[♯] Note that the underlying atomistic structure for Al is always fcc, even if the constructed triangulation is sc.

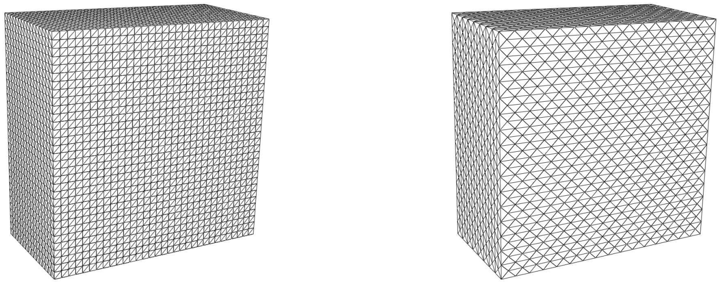

(a) $N_h = 35937$, $1/n'_h = 0.2617$ (b) $N_h = 17969$, $1/n'_h = 0.1290$

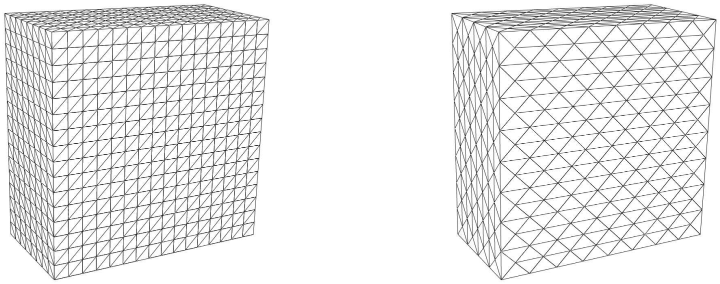

(c) $N_h = 4913$, $1/n'_h = 0.0358$ (d) $N_h = 2457$, $1/n'_h = 0.0179$

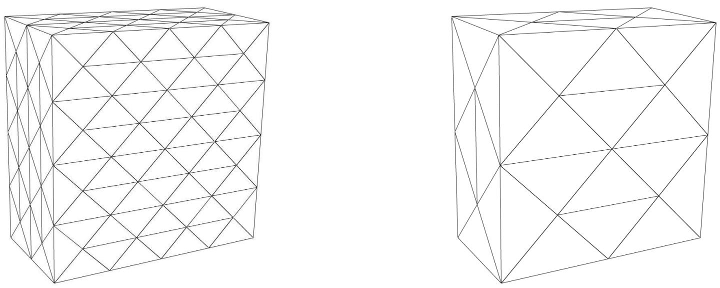

(e) $N_h = 365$, $1/n'_h = 0.0027$ (f) $N_h = 63$, $1/n'_h = 0.0005$

Figure 3. Mid-section cut of the relaxed $32a_0 \times 32a_0 \times 32a_0$ system for several mesh coarsenings.

excursions about $V/V_0 = 1$ are observed. The slope of the curves (directly proportional to the thermal expansion coefficient) also diminishes with increasing mesh size. Second, cluster size has little or no effect on the temperature behavior of the system's volume.

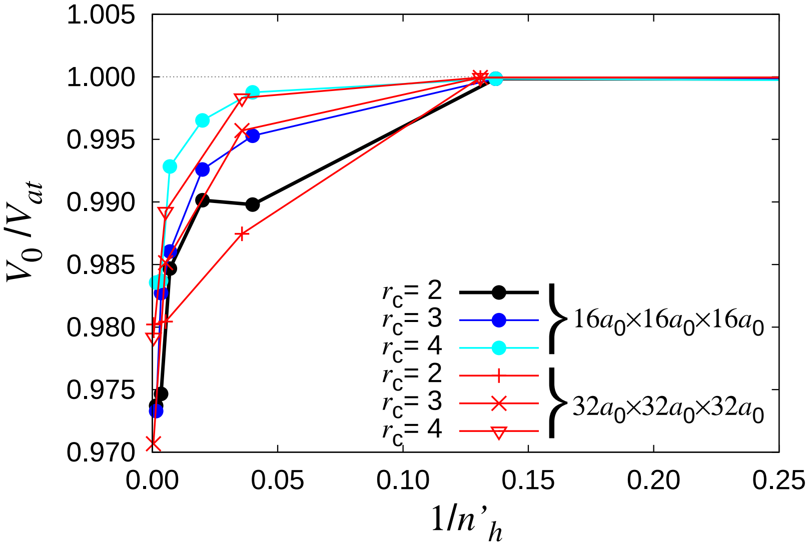

Figure 4. Normalized equilibrium volume V_0 as a function of the nomalized number of representative atoms. The volumes are calculated via conjugate-gradient energy minimizations and are normalized to the relaxed volumes of the atomistic systems of 2.662×10^5 and 2.138×10^6 Å^3 for the $16a_0 \times 16a_0 \times 16a_0$ and $32a_0 \times 32a_0 \times 32a_0$ systems respectively. The unrelaxed volumes (corresponsding to an infinite system) in each case are 2.685×10^5 and 2.148×10^6 Å^3.

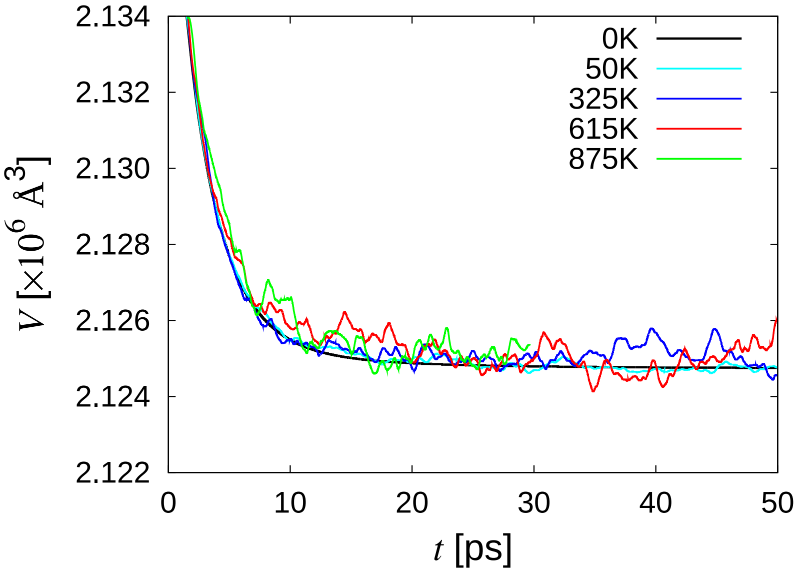

Figure 5. Time evolution of the system volume at five different temperatures for the (N=137313, N_h=729, r_c=4) system. Measurements start only after steady state is assumed to be reached at 25 ps. In all cases, simulations are initialized from the unrelaxed state with zero kinetic energy.

358 Similar conclusions can be extracted for the $16a_0 \times 16a_0 \times 16a_0$ data. The thermal

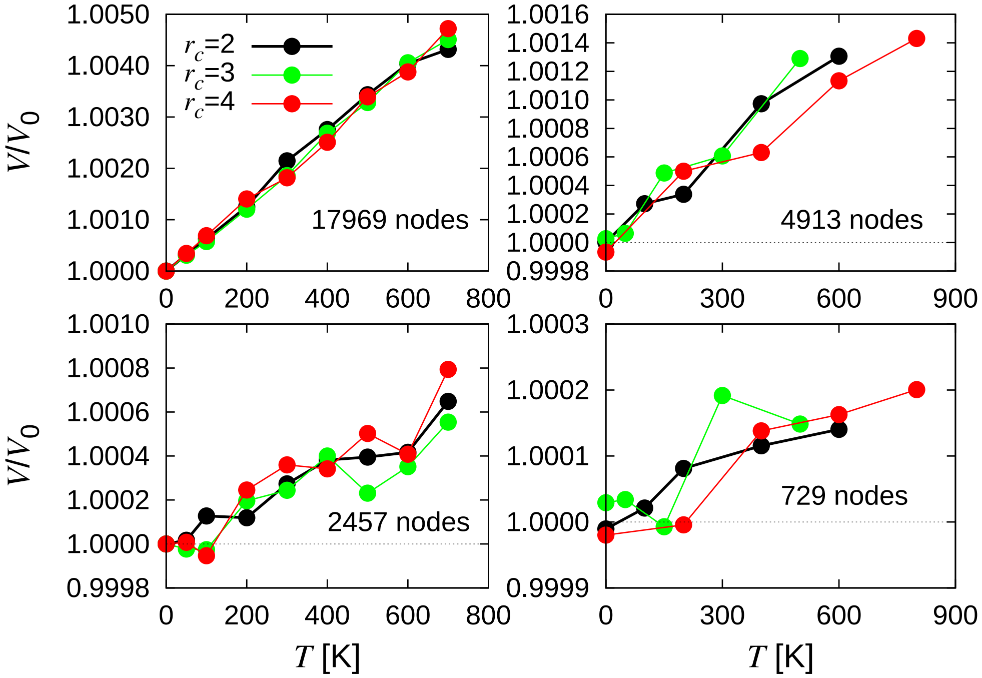

Figure 6. Thermal expansion behavior of a $32a_0 \times 32a_0 \times 32a_0$ Al system containing 137313 lattice sites for four mesh sizes. Results in all cases are given for three different cluster sizes. The expected linear expansion behavior deteriorates progressively as the mesh is coarsened.

expansion behavior for this system is provided in Fig. 7 for four representative meshes. Linear V-T dependencies are clearly established for the 4913 and 729-node cases, whereas less well-defined trends are observed for the higher coarsening cases of 125 and 27 nodes. As for the $32a_0 \times 32a_0 \times 32a_0$ samples, the cluster size has little or no influence on the measured volumetric expansion. All the numerical calculations carried out for this system are also given in Table 3.

The calculated values of α compiled in Table 3 are plotted in Figure 8 as a function of the average number of atoms represented by each node n'_h. Clearly, for low values of $n'_h(\leqslant 50)$, the cluster size dependence is practically nonexistent. For larger values, representative of coarser meshes, some uncorrelated varibility appears. Regarding the correlation between the thermal expansion coefficient and the mesh size, we refer to the derivation carried out in Section 3.5. The summation in eq. (49) implies that a linear relation exists between α and N_h. This means that α should vanish when N_h goes to zero, or, in other words, when n'_h approaches infinity. Additionally, in the atomistic limit ($n'_h = 1$), the thermal expansion coefficient must be equal to that calculated in Fig. 2. Consequently, we try a fitting function of the form $\alpha(n'_h) = a/{n'_h}^b$, where a and b are fitting constants. The physical meaning of a is clear from this discussion: $a \equiv \alpha(1) \equiv \alpha_{\rm at}$. It is not clear *a priori* what the value of b should be, although $b = 1$ would suffice to meet the above conditions.. In any case, after considering for the sake of accuracy a subset of the data in Table 3 corresponding to

Table 3. Compilation of all the thermal expansion coefficient data (in K^{-1}) for the $16a_0 \times 16a_0 \times 16a_0$ (17989 lattice sites) and $32a_0 \times 32a_0 \times 32a_0$ (137313 lattice sites) Al systems obtained from dynamic simulations as a function of the mesh and cluster sizes. The mesh size is expressed as both the number of nodes N_h and the approximate number of lattice sites represented per node (N/N_h). We note that, for the fully-atomistic systems, $\alpha = 1.72 \times 10^{-5}$ and 1.70×10^{-5} K^{-1}, respectively.

	Mesh size		Cluster size		
	N_h	$\frac{N}{N_h}$	2	3	4
$16a_0 \times 16a_0 \times 16a_0$	27	666.3	2.60×10^{-8}	7.61×10^{-9}	2.90×10^{-8}
	125	143.9	4.19×10^{-8}	3.53×10^{-8}	3.21×10^{-8}
	365	49.3	2.76×10^{-7}	1.37×10^{-7}	3.64×10^{-7}
	729	24.7	6.12×10^{-7}	8.55×10^{-7}	7.51×10^{-7}
	2457	7.3	2.29×10^{-6}	2.12×10^{-6}	2.14×10^{-6}
	4913	3.7	4.49×10^{-6}	4.35×10^{-6}	4.42×10^{-6}
$32a_0 \times 32a_0 \times 32a_0$	729	188.4	7.24×10^{-8}	6.61×10^{-8}	8.53×10^{-8}
	2457	55.9	2.80×10^{-7}	2.48×10^{-7}	3.44×10^{-7}
	4913	27.9	7.41×10^{-7}	8.25×10^{-7}	6.05×10^{-7}
	17969	7.6	2.17×10^{-6}	2.22×10^{-6}	2.20×10^{-6}
	35937	3.8	4.10×10^{-6}	–	–

a cluster size of $r_c = 4$ (including both sample sizes), the least-squares fitting results in $\alpha(n'_h) = 1.53 \times 10^{-5} {n'_h}^{-0.97}$. The results for a and b are in excellent agreement with their rationalized values. Adding any other subset of the data in Table 3 only results in small deviations of a and b obtained for $r_c = 4$. It is worth noting, however, that the $16a_0 \times 16a_0 \times 16a_0$ results appear to indicate the existence of two regimes, both characterized by the same exponent $b \approx 1$ but with slightly different prefactors. The one below $n'_h \approx 50$ yields the same value for a as the $r_c = 4$ data, whereas the one above is about 10% lower. On the basis of the results shown in Figs. 7 and 6, where for coarser meshes the linear behavior of α is poorly established, we simply attribute this effect to noise in the thermal expansion measurements and assume that all the data follow the same physical behavior with sporadic excursions due to numerical error.

We emphasize that for $n'_h = 1$ we recover the atomistic thermal expansion coefficient from a data set that includes meshes of varying coarseness but not the fully atomistic configuration. This is an important and encouraging result, for it implies that the thermal expansion limit is naturally recovered from dynamic QC simulations, and that α is inversely proportional to the *weight* of the representative atoms. Evidently, in the limit of an infinitely coarse mesh α tends to zero, as there are no vibrational DOF to support any volumetric expansion. It is hence verified that, $\forall\ n'_h \in [1, \infty)$:

$$\lim_{n'_h \to 0} \alpha(n'_h) = \alpha_{\mathrm{at}}$$

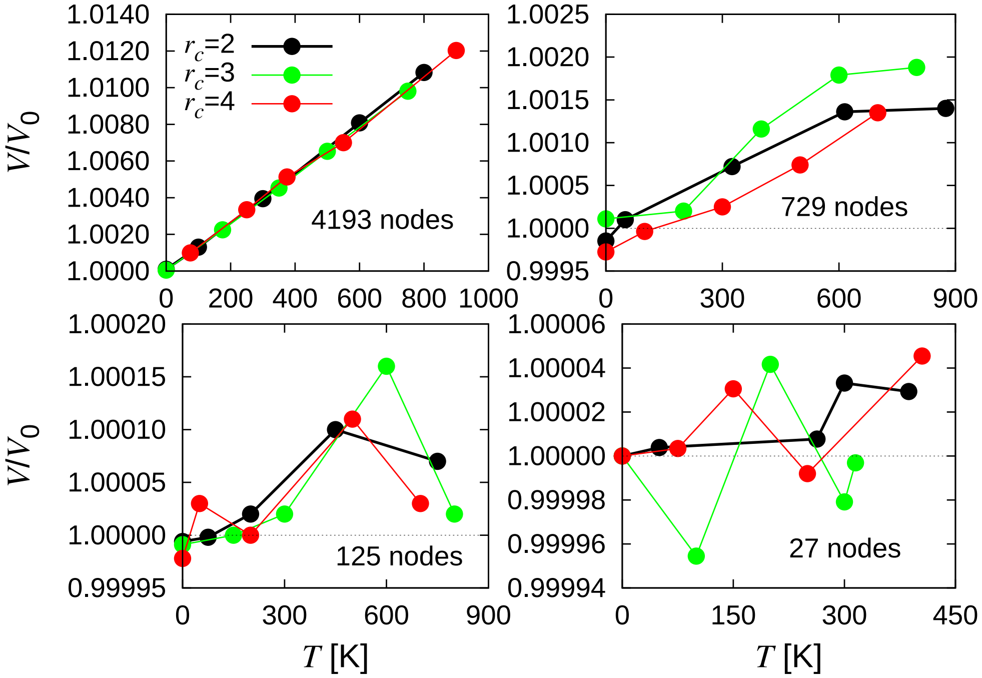

Figure 7. Thermal expansion behavior of a $16a_0 \times 16a_0 \times 16a_0$ Al system containing 17989 lattice sites for four mesh sizes. Results in all cases are given for three different cluster sizes. The expected linear expansion behavior deteriorates progressively as the mesh is coarsened.

and

$$\lim_{n'_h \to \infty} \alpha(n'_h) = 0$$

The behavior of α shown in Fig. 8 also suggests that it does not depend on the total system size. This implies that our $16a_0 \times 16a_0 \times 16a_0$ and $32a_0 \times 32a_0 \times 32a_0$ samples are beyond the scattering limit where the population of bulk phonons is sufficiently high to outweigh non-periodic surface phonons [66]. Above this limit, which we have not established here, one would presumably find that a single universal relation governs the dependence of the thermal expansion coefficient with the mesh size. In that regime, the difference $|\alpha_{\mathrm{at}} - \alpha(n'_h)|$ can be used as an error estimator of the total entropy of the coarsened system, which could be used for re-scaling purposes.

4.1.2. Thermal expansion from free-energy calculations in the quasiharmonic approximation.

In this section we rationalize the results obtained via direct dynamic QC simulations in Section 4.1 utilizing the theoretical framework derived in Section 3.5. Our objective is to recover the thermal expansion coefficient attendant to each (N, N_h, r_c) system purely from fundamental crystal properties.

To evaluate the volume derivatives in eq. (49) we use the following approach. First, we compute F_h-θ curves using eq. (46) at several temperatures. We sample a sufficient number of points to ensure that the equilibrium volume is enclosed in the volume range

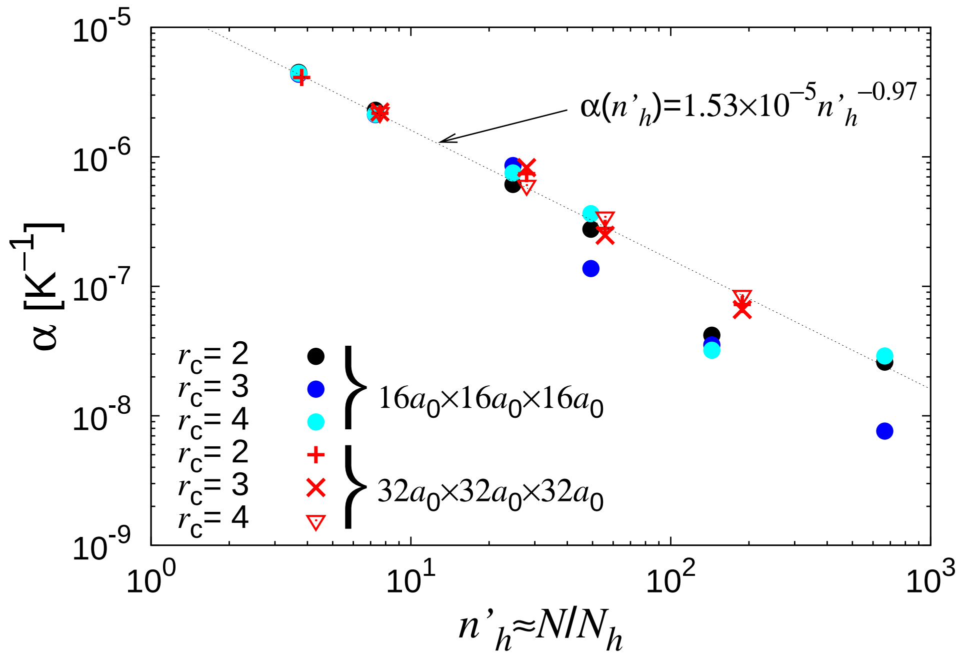

Figure 8. Thermal expansion coefficient as a function of the approximate nodal weights. The dashed line is a least-squares fit of the form $\alpha(n_h) = a/{n_h}^b$ (where a and b are constants) to the data corresponding to $r_c = 4$ for both sample sizes.

explored. As shown in Section 3.5, in this case V is linear in T, so that we simply fit the *locus* of the temperature-dependent equilibrium volumes to eq. (52). In this fashion, the Grüneisen parameter is calculated indirectly for each (N, N_h, r_c) system and the thermal expansion coefficient can be readily obtained. This approach requires that both the internal energy, $\Phi_h(\mathbf{0}, \theta)$ in eq. (46), and the vibrational density of states (vDOS), obtained via eq. (37), be calculated as a function of volume for each one of the systems considered.

To test the validity of this approximation, we first calculate the atomistic thermal expansion coefficient and compare it to the value of $\alpha_{\mathrm{at}} = 1.79 \times 10^{-5}\ \mathrm{K}^{-1}$ given by Ercolessi and Adams [63]. The vibrational spectra for a periodic 4000-atom system are given in Fig. 9(a) as a function of the linear dimensional change a/a_0 ††. We can see that expansion results in a 'redshift', *i.e.* a narrowing of the normal frequency band toward lower energies.

With this information we then calculate $F_h(T, a/a_0)$ and plot it in Fig. 10(a) at a number of temperatures. From second-order polynomial fits to the data at each temperature we obtain the equilibrium lattice constant a at each temperature. The temperature dependence of these equilibrium lattice parameters (assumed linear, see Fig. 10(a), r.h.s.) gives the linear expansion coefficient, which for this calculation is $1.79 \times 10^{-5}\ \mathrm{K}^{-1}$, in perfect agreement with the value obtained by Ercolessi and Adams

[††] Note that $V/V_0 \approx 3a/a_0$, and $\theta = \Delta V/V_0 \approx 3\Delta a/a_0$.

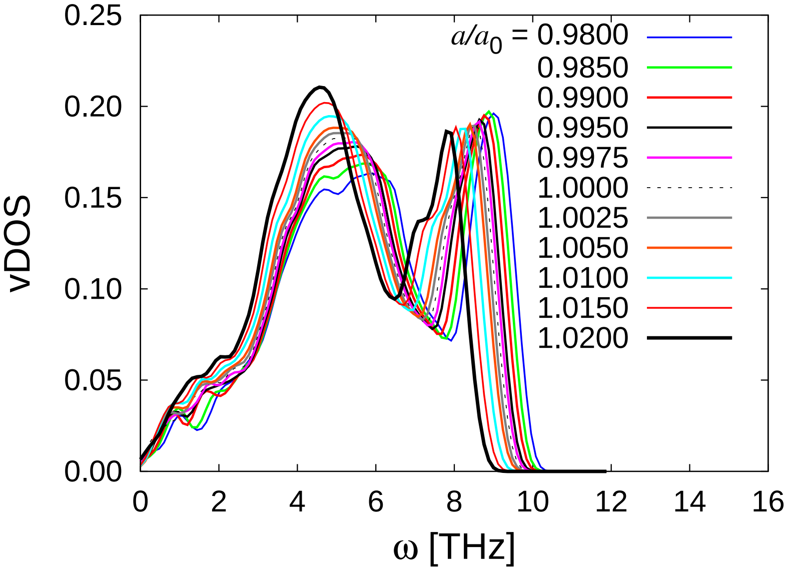

(a) Periodic system with 4000 atoms representing bulk Al

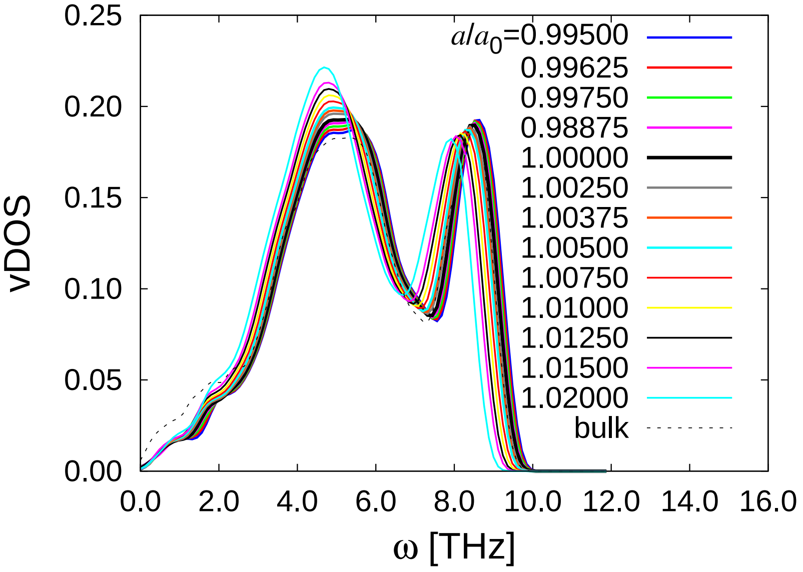

(b) Finite system with constrained surfaces, similar to those simulated by QC, containing 4631 atoms

Figure 9. Normalized vDOS as a function of the normalized lattice parameter a/a_0 for cubic $10 \times 10 \times 10a_0$ Al crystallites with different boundary conditions. Volumetric expansion results in a narrowing of the populated frequency band. The dashed curve represents the same system in both subfigures.

from MD simulations.

This result confirms the validity of the quasiharmonic approximation for Al and allows us to undertake the coarse-mesh calculations with confidence. However, for further verification, we now repeat this calculation for a $10a_0 \times 10a_0 \times 10a_0$ finite system (4631 atoms) with free boundaries, akin to those used in QC simulations. The volume-

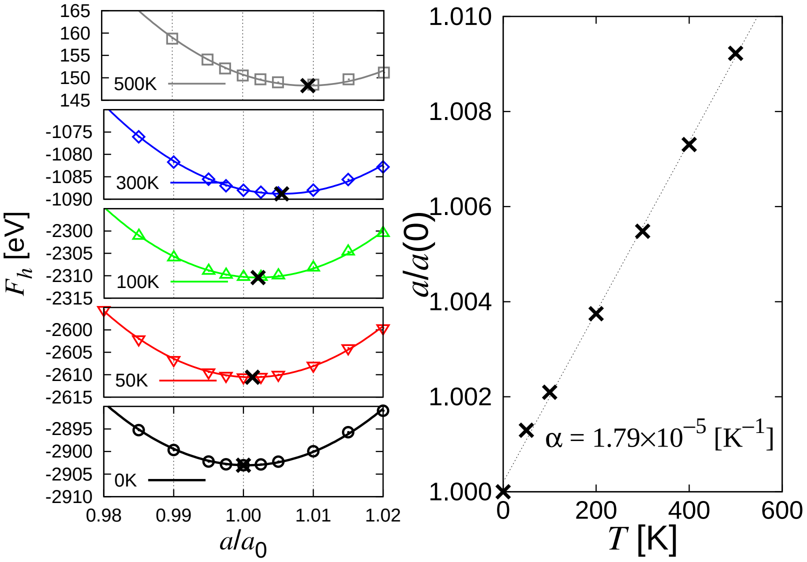

(a) Bulk (periodic) $10a_0 \times 10a_0 \times 10a_0$ cell.

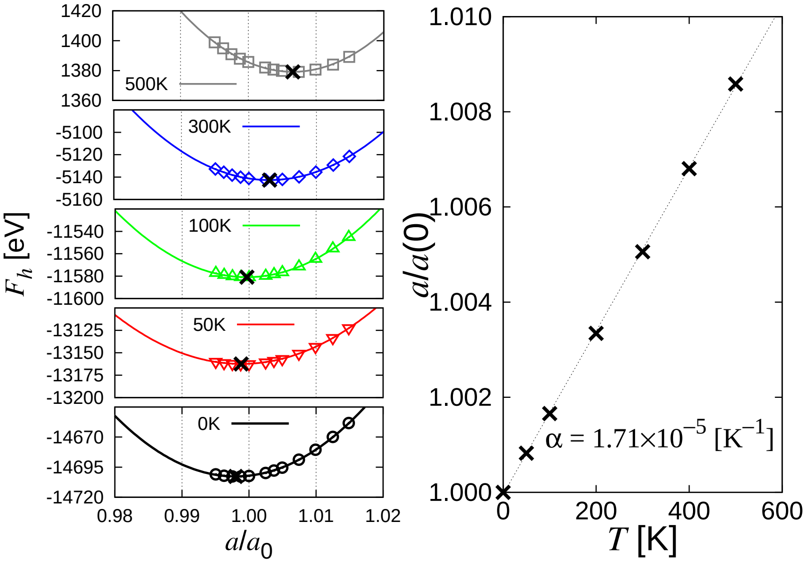

(b) Finite (constrained surfaces) $10a_0 \times 10a_0 \times 10a_0$ cell.

Figure 10. (Left) Free energy as a function of the normalized lattice parameter at five representative temperatures for fully atomistic Al systems. The minima of the fitted 2$^{\mathrm{nd}}$-order polynomials (marked with a black 'x') are the equilibrium lattice parameter at each temperature, normalized to the bulk a_0 of 4.032 Å. (Right figure) Temperature dependence of the equilibrium lattice parameter. The derivative of the linear fit to the data gives the thermal expansion coefficient. The results are normalized in each case to the lattice parameter $a(0)$ that gives the equlibrium volume at 0K, *i.e.* 4.032 and 4.021 Å, respectively.

dependent eigenfrequencies are again given in Fig. 9(b), whereas the quasiharmonic analysis is shown in Fig. 10(b). This time, the calculation yields $\alpha = 1.71 \times 10^{-5}$ K^{-1}, which is in excellent agreement with the the value of $\alpha = 1.70 \sim 1.72{\times}10^{-5}$ K^{-1} obtained directly from QC dynamical simulations in Fig. 2. Although here we are concerned with system containing 17969 and 137313 atoms, the size of the dynamical matrices that can be diagonalized ($3N_h \times 3N_h$) is restricted to $\approx (13,500 \times 13,500)$. However, as for the simulations carried out in Section 4.1.1, the good agreement between this calculation for the $10a_0 \times 10a_0 \times 10a_0$ sample and the results obtained for the $16a_0 \times 16a_0 \times 16a_0$ and $32a_0 \times 32a_0 \times 32a_0$ sytems suggests that we are beyond the limit where surface effects depend on length scale. Thus, this value of $\approx 1.71 \times 10^{-5}$ K^{-1} constitutes our reference baseline against which all the coarse systems to be studied subsequently are benchmarked.

Having confirmed the validity of the approach described in Section 3.5, we now study mesh and cluster size effects according to Section 3.4. First, we compute the vibrational DOS for different coarse systems, *i.e.* $n'_h \neq 1$, and, subsequently, calculate α by the procedure described in Fig. 10. The DOS for all the $(17969, N_h, r_c)$ systems considered in this work are given in Fig. 11 as a function of cluster and mesh size.

The thermal expansion coefficients associated with these meshes are given in table 4. The number of cases for the $32a_0 \times 32a_0 \times 32a_0$ system is again limited by the size of the dynamical matrices that can be diagonalized. Therefore, here, we calculate α only for $n'_h = 188.4$ and 55.9 (729 and 2457 nodes).

Table 4. Thermal expansion coefficients (in K^{-1}) calculated within the quasiharmonic approximation for the systems considered in Table 3. '–' symbols indicate that the diagonalization of the corresponding dynamical matrices was beyond our computational capabilities.

	Mesh size		Cluster size		
	N_h	n'_h	2	3	4
$16a_0{\times}16a_0{\times}16a_0$	27	666.3	7.28×10^{-8}	4.33×10^{-8}	4.88×10^{-8}
	125	143.9	1.81×10^{-7}	2.09×10^{-7}	1.55×10^{-7}
	365	49.3	4.06×10^{-7}	3.77×10^{-7}	3.52×10^{-7}
	729	24.7	8.92×10^{-7}	8.30×10^{-7}	8.11×10^{-7}
	2457	7.3	2.50×10^{-6}	2.35×10^{-6}	2.35×10^{-6}
	4913	3.7	–	–	–
$32a_0{\times}32a_0{\times}32a_0$	729	188.4	1.27×10^{-7}	1.19×10^{-7}	1.21×10^{-7}
	2457	55.9	3.71×10^{-7}	3.46×10^{-7}	1.03×10^{-6}
	4913	27.9	–	–	–
	17969	7.6	–	–	–
	35937	3.8	–	–	–

The results obtained thus far suggest that cluster size has a negligible impact on the thermal expansion behavior of the tested coarse Al samples (cf. Figs. 7, 6 and 8). In fact,

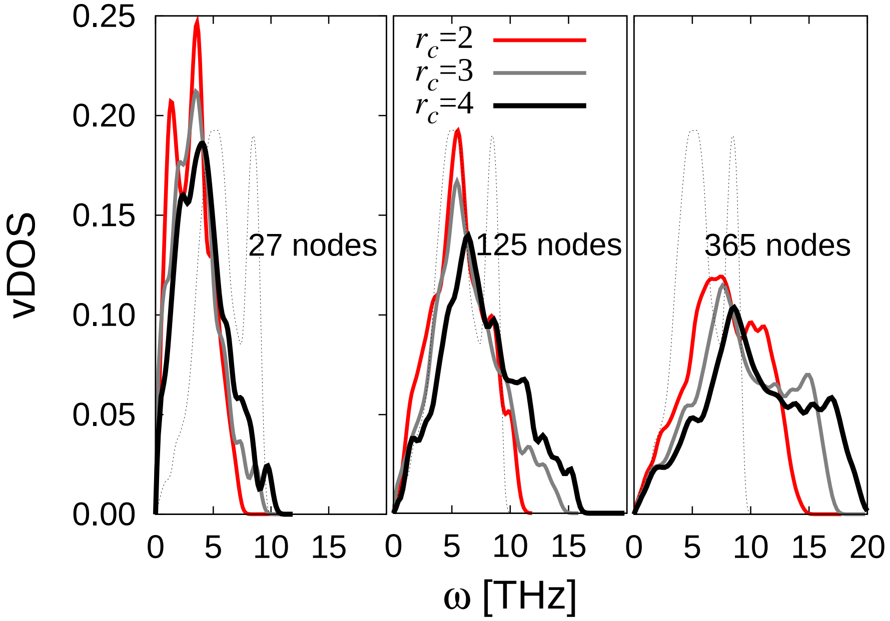

(a) Vibrational DOS for systems with 27, 215 and 365 nodes ($n'_h = 666.3$, 143.9 and 49.3 respectively).

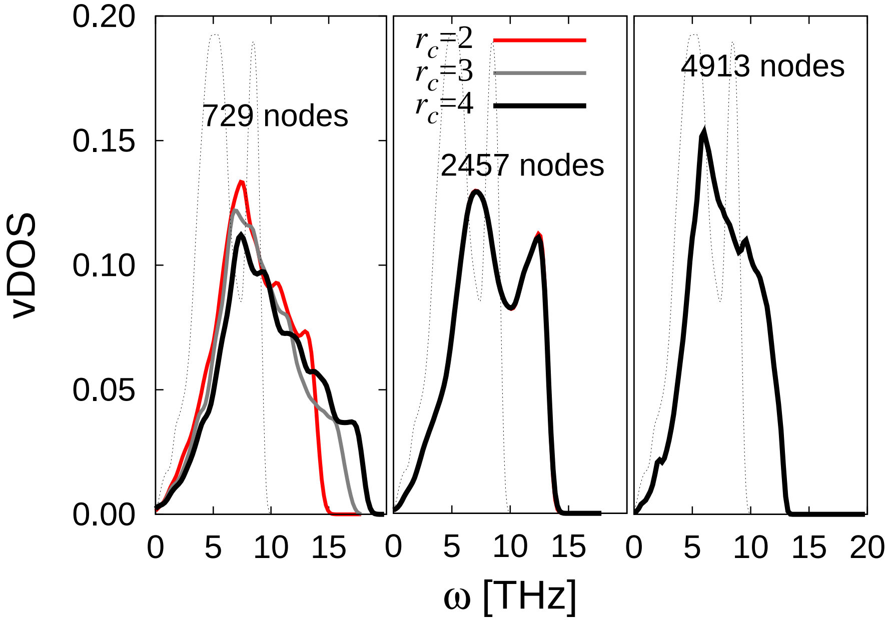

(b) Vibrational DOS for systems with 729, 2457 and 4913 nodes ($n'_h = 24.7$, 7.3 and 3.7 respectively).

Figure 11. Normalized vibrational spectra for different $(17969, N_h, r_c)$ systems. Superimposed for comparison is the DOS for the atomistic system.

cluster size is seemingly only important in the context of static energy minimizations (cf. Figs. 4 and 11). However, eqs. (42) and (43) imply a direct correspondance of the normal modes of vibration with h and r_c. This correspondence is multiplicatively composed of a $(r_c/h)^3$ term derived from the nodal masses, and an undefined dependence through the force constants. We next study these two contributions separately.

4.1.3. Analysis of mesh and cluster effects on the entropy of QC systems. Let us now briefly return to Fig. 11, from which several interesting observations can be extracted. First, as expected from eq. (43), there is a direct correlation between r_c and the *hardness* of the vibrational spectra for each mesh. Cluster overlap at large values of ${n'}_h$ —*i.e.* relatively fine meshes— results in identical dynamical matrices. This is the reason why, for $N_h = 2457$ (for $r_c = 3$, 4) and 4913 (for all r_c), the DOS is independent of r_c. Evidently, the corresponding thermal expansion coefficients shown in Table 4 are also independent of the cluster size. This behavior is also captured within numerical error in the dynamic simulations of α by the (17969, 2457/4913, r_c) and (137313, 17969, r_c) systems (cf. Table 3). Assuming, as eq. (43) indicates, that the vibrational spectra are shifted with respect to one another by a factor $\lambda \propto r_c^p$, we calculate in Table 5 the average shift for each mesh considered in Table 4. λ is calculated as the ratio between the characteristic frequencies, $\tilde{\omega}$, of the vDOS corresponding to each cluster size. To first order, $\tilde{\omega}$ can be identified with the mean of each vibrational distribution given in Fig. 11, which are given in Table 5. The data suggests that the exponent to which r_c is elevated ranges between $p = 0.55$ and 1.15. It is certainly lower than the *weight factor* $r_c^{1.5}$ given in eq. (43), suggesting that the force constants may govern how the vibrational properties of a given mesh vary with cluster size. Regarding mesh size effects, the weight factor from eq. (43) again suggests an $\omega \propto h^{-1.5}$ dependence. However, the calculated $\tilde{\omega}$ display the curious behavior shown in Fig. 12(a), characterized by a maximum at ${n'}_h \approx 50$. For larger meshes, the mean frequency decreases as ${n'}_h^{-0.37}$, whereas in the

Table 5. Average eigenfrequencies (in THz), $\tilde{\omega}$, and relative 'shift', λ, of the DOS of all the $16a_0 \times 16a_0 \times 16a_0$ meshes. λ is computed as the ratio between the average eigenfrequencies of each DOS. Note that $r_c(3)/r_c(2) = 1.225a_0/a_0 = 1.22$, $r_c(4)/r_c(3) = 1.414a_0/1.225a_0 = 1.15$, and $(r_c(3)/r_c(2))^{3/2} = 1.36$ and $(r_c(4)/r_c(3))^{3/2} = 1.24$. The cases where there is cluster overlap are separated by a dashed line. The full atomistic case is shown at the end of the table for reference.

N_h	n'_h	$\tilde{\omega}\vert_{r_c=2}$	$\tilde{\omega}\vert_{r_c=3}$	$\tilde{\omega}\vert_{r_c=4}$	$\lambda_{2\to3} = \frac{\tilde{\omega}\vert_{r_c=3}}{\tilde{\omega}\vert_{r_c=2}}$	$\lambda_{3\to4} = \frac{\tilde{\omega}\vert_{r_c=4}}{\tilde{\omega}\vert_{r_c=3}}$
27	666.3	3.14	3.52	4.11	1.12	1.16
125	143.9	5.59	6.38	7.48	1.14	1.17
365	49.3	7.70	9.22	10.39	1.19	1.12
729	24.7	8.40	8.93	9.79	1.06	1.10
2457	7.3	8.44	8.44	8.44	1.00	1.00
4913	3.7	7.57	7.57	7.57	1.00	1.00
atomistic	1.0	5.59	5.59	5.59	1.00	1.00

range where there is cluster overlap the mean frequency (slightly) increases with mesh size. This is a most puzzling observation, as it is well known that finer meshes can support higher-frequency vibrations. This again may be related to the force constant term in eq. (43), whose cluster and mesh dependencies we set out to study.

Force constants are categorized according to their direction and the nearest neighbor shell they correspond to. Here, we restrict ourselves to the largest force constant for a given mesh, as these are the ones which result in the highest vibrational frequencies. Generally, the largest force constants correspond to first-nearest neighbor distances and directions, ϕ_{11}[†].

Of course, in different crystal lattices —*e.g.* fcc and sc— ϕ_{11} does not necessarily correspond to the same direction and/or distance. For example, in sc systems, ϕ_{11} is along the $\langle 100 \rangle$ direction, whereas in fcc crystals it is defined for the $\langle 110 \rangle$ direction. In our QC systems with sc meshes ϕ_{11} is indeed the largest force constant observed. However, in the fcc meshes, we have seen that the force constants along the second nearest neighbor direction, ϕ_{21}, are roughly three times larger than ϕ_{11}. Therefore, we study the mesh and cluster size dependencies of ϕ_{11} and ϕ_{21} for, respectively, sc and fcc triangulations. The results are shown in Fig. 12(b), where, in accordance with eq. (43), we plot the values of $\sqrt{\phi}$. It can be immediately seen that, from a qualitative standpoint, the mesh dependence of the force constants mirrors that of $\tilde{\omega}$. The characteristic exponent of the power law fit to the three largest meshes is -0.20. Assuming that the characteristic exponent of $\tilde{\omega}$ results from the combination of a force constant plus a mass factor, we have that the latter is $-0.37-(-0.20) = -0.17$, far from the $h^{-1.5}$ dependence extracted from eq. (43). The behavior for finer meshes remains unexplained, an issue that we shall discuss in the following section.

In any case, we conclude that the force constant term is the dominating one in eq. (43) and explains the unusual behavior in the DOS (Fig. 11) of the studied meshes. Nevertheless, the impact of this anomalous behavior on the thermal expansion coefficient is negligible in view of the calculated data in Table 4. This is owed to the reduced summation space in eq. (49), and to the fact that the derivatives of the eigenfrequencies with respect to $(1-\theta)$ are seemingly not affected by this phenomenon. As well, we do not discard the possibility that this effect, extracted from static calculations, does not manifest itself during the course of dynamical simulations.

4.2. Tantalum results.

4.2.1. Thermal expansion from dynamic simulations. As a representative bcc material for this study we have chosen Ta, for which some experience using static QC exists [27]. Ta is modeled using the EAM potential developed by Li *et al* [67], which has been fitted to an experimental equation of state that includes data at 10% compression.

[†] Here we follow the standard notation where the first subindex refers to the nearest-neighbor shell and the second one to represent whether the force constant is longitudinal ('1') or transversal ('2' or '3').

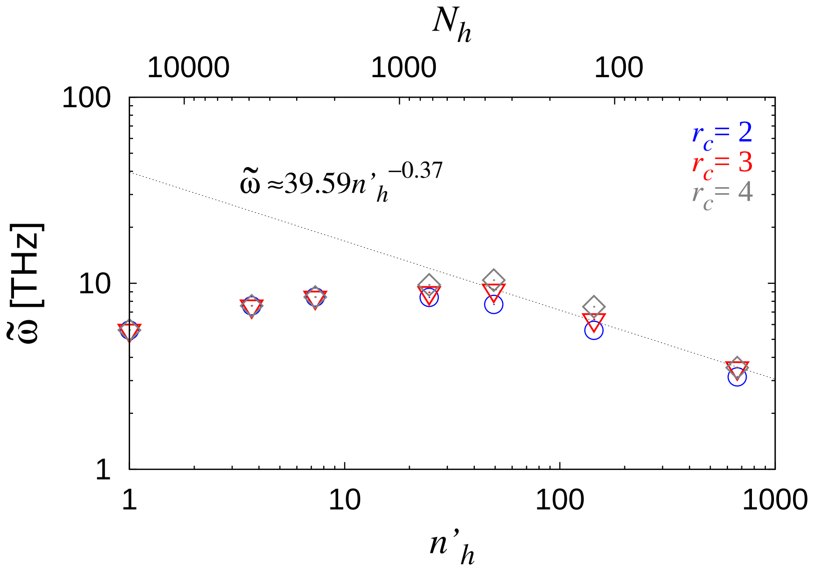

(a) Variation of the mean eigenfrequency with mesh size.

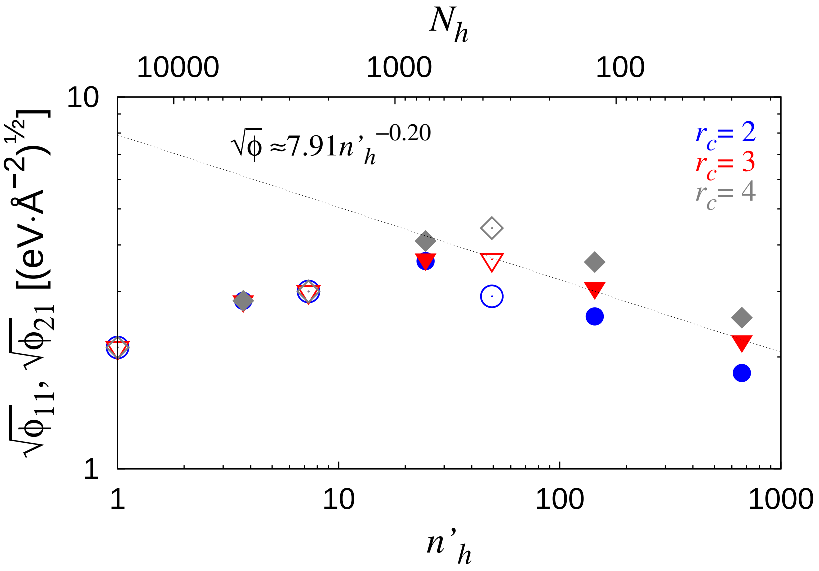

(b) Force constants as a function of mesh size. Solid symbols correspond to simple cubic nodal meshes, while open symbols represent fcc meshes. In each case, we plot the largest force constant that appears in the crystal, regardless of the nearest neighbors shell they correspond to (ϕ_{21} for sc structures, and ϕ_{11} for fcc).

Figure 12. Mesh dependences of the mean eigenfrequencies and force constants for the $16a_0 \times 16a_0 \times 16a_0$ system. The dotted line corresponds to power law fits to the three largest meshes, with characteristic exponents of -0.37 for $\tilde{\omega}$ and -0.20 for $\sqrt{\phi}$.

Figure 13 shows the temperature dependence of the Ta lattice parameter for a periodic system using molecular dynamics [67] compared to the experimental data points given by Touloukian *et al* [60]. The atomistic data show inverse thermal expansion below 298K, which is an artifact of the interatomic potential [67]. As the third-degree polynomial fits show, the thermal expansion coefficient displays a strong temperature dependence. Between 500 and 1500K —where a reasonably linear dependence is found—, Touloukian *et al* give a value of $\alpha = 7.79 \times 10^{-6}$ K^{-1}, whereas the MD results suggest a value of 6.02×10^{-6} K^{-1}. As T increases, however, this agreement is lost and the differences become more pronounced.

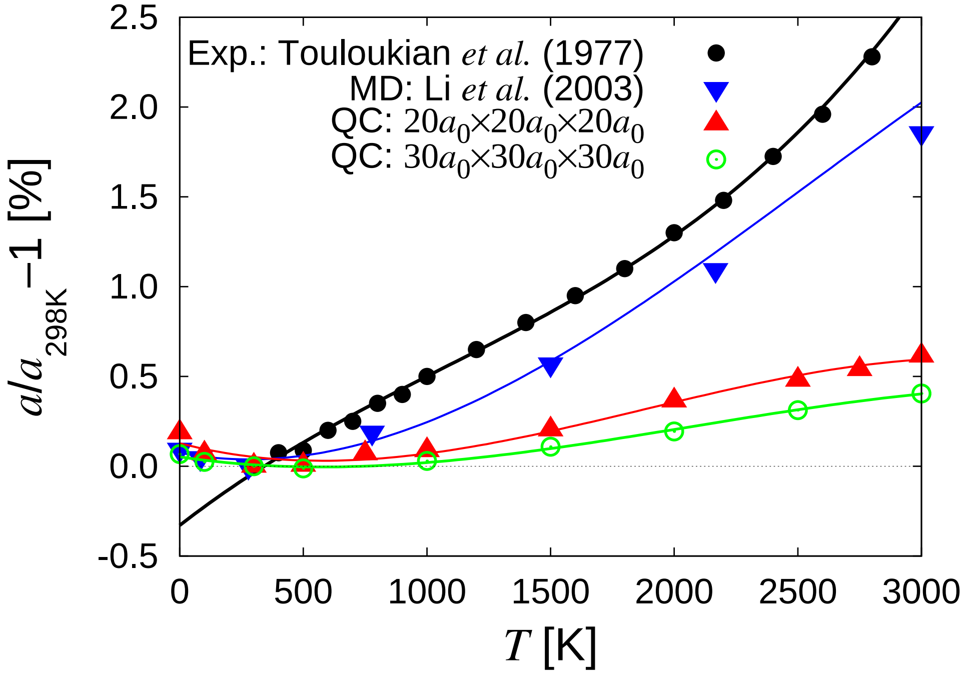

Figure 13. Variation of the bcc Ta lattice parameter with temperature comparing four different cases. The solid dots correspond to the experimental data above 298K given by Touloukian *et al* [60]. Inverted triangles are MD calculations for a periodic system performed by Li *et al* [67]. Finally, the solid triangles and open dots correspond to QC dynamic simulations at zero pressure of finite $20a_0 \times 20a_0 \times 20a_0$ and $30a_0 \times 30a_0 \times 30a_0$ systems. All the data are normalized to the value of a_0 at 298K. Solid lines are third-degree polynomial fits to the data.

For our dynamic QC study, we have analyzed finite $20a_0 \times 20a_0 \times 20a_0$ (17261 atoms) and $30a_0 \times 30a_0 \times 30a_0$ (56791 atoms) finite systems. As for Al, we start by obtaining the corresponding atomistic thermal expansion behavior. Results are also shown in Figure 13, where several features are noteworthy. First, thermal expansion in finite systems is considerably suppressed with respect to the periodic (infinite) sample. Second, both curves reproduce the artificial negative thermal expansion coefficient below room temperature. Additionally, at high temperatures, the behaviors of the $20a_0 \times 20a_0 \times 20a_0$ and $30a_0 \times 30a_0 \times 30a_0$ systems gradually diverge. The polynomial fits to the QC data are given in Table 6. The average thermal expansion coefficient in the $1000 < T < 2000$K interval is, respectively, 4.14×10^{-6} and 2.36×10^{-6} K^{-1}. These now constitute our reference values for the coarse QC simulations.

Table 6. Coefficients of the third degree polynomials $[a(T)/a(298\text{K}) - 1] = aT^3 + bT^2 + cT + d$ for the data from dynamic QC simulations plotted in Fig. 13. The linear thermal expansion coefficient is calculated as: $\alpha(T) = 3aT^2 + 2bT + c$.

Sample size	a	b	c	d
$20a_0 \times 20a_0 \times 20a_0$	-6.52×10^{-13}	3.67×10^{-9}	-3.59×10^{-6}	1.28×10^{-3}
$30a_0 \times 30a_0 \times 30a_0$	-3.37×10^{-13}	2.09×10^{-9}	-2.07×10^{-6}	5.23×10^{-4}

The discrepancies observed between the two finite systems studied and the periodic one could indicate that surface effects are non-negligible in this case. This is further substantiated by the difference between the $20a_0 \times 20a_0 \times 20a_0$ and $30a_0 \times 30a_0 \times 30a_0$ systems themselves. Next, we examine the thermal expansion behavior of gradually coarser meshes. The calculated database for Ta is not as extensive as for Al, and only three meshes are studied for the $20a_0 \times 20a_0 \times 20a_0$ sample and four for the $30a_0 \times 30a_0 \times 30a_0$ one. Figures 14 and 15 show the respective thermal expansion behaviors using three cluster sizes. In the bcc lattice, r_c=2, 3, 4 correspond to nearest neighbor shells within a distance of a_0, $1.414a_0$ and $1.658a_0$, containing 14, 26 and 50 atoms, respectively.

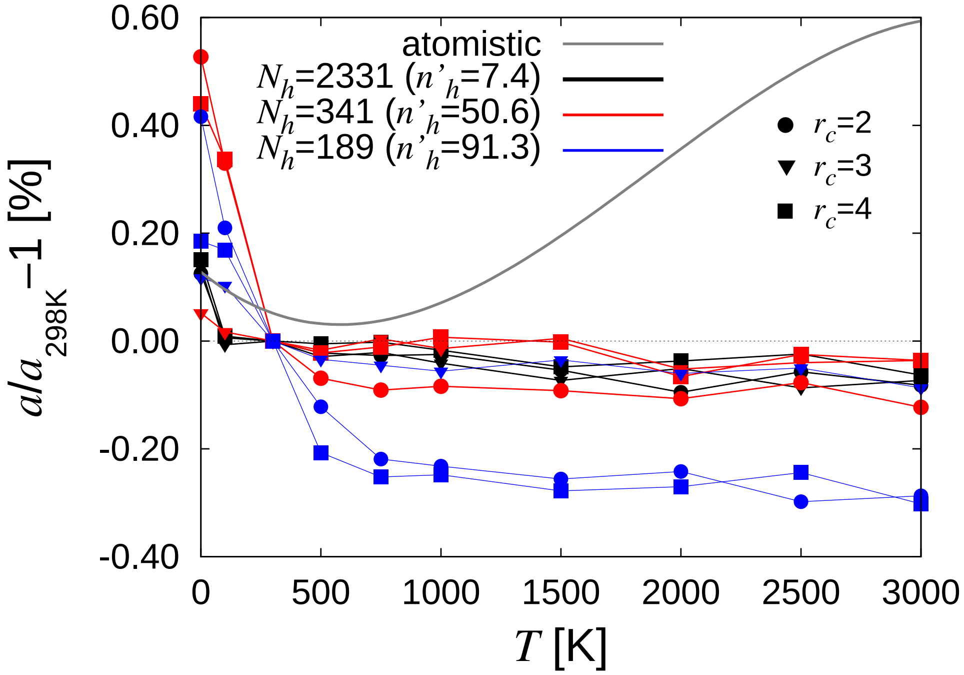

Figure 14. Thermal expansion behavior of the $20a_0 \times 20a_0 \times 20a_0$ system (17261 lattice sites). Three meshes, with three cluster sizes each, are considered. All meshes show negative thermal expansion until approximately 500K, at which point the lattice parameter becomes independent of T ($\alpha = 0$). We recall that $n'_h = N/N_h$ is the *effective* nodal weight.

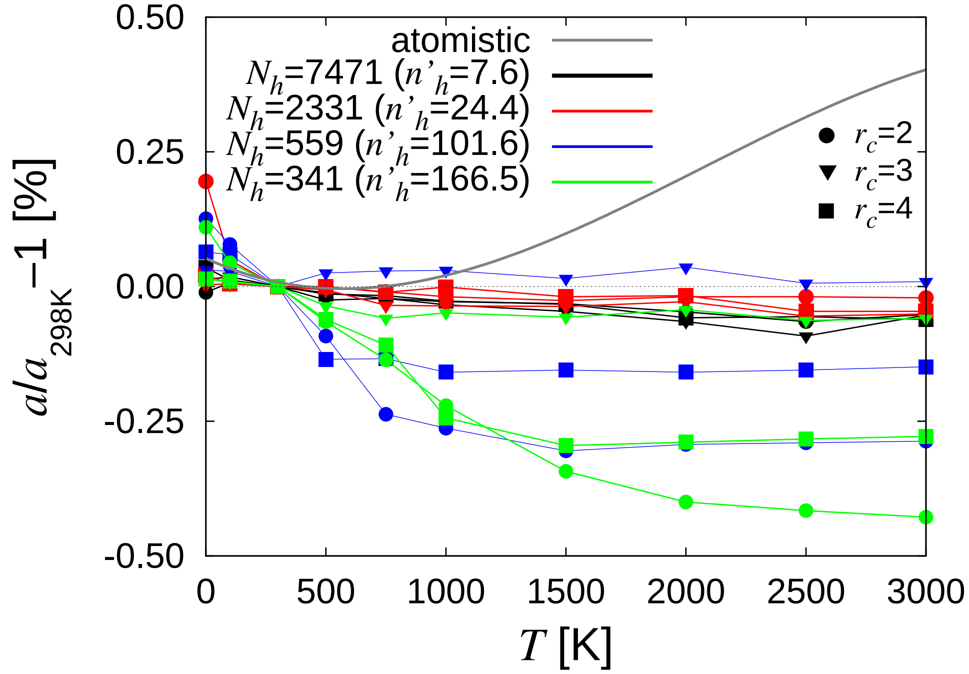

Figure 15. Thermal expansion behavior of the $30a_0 \times 30a_0 \times 30a_0$ system (56791 lattice sites). Four meshes, with three cluster sizes each, are considered. All meshes show negative thermal expansion until approximately 1000K, after which the lattice parameter becomes independent of T ($\alpha = 0$).

The following general observations can be extracted from both figures:

- All meshes display negative thermal expansion behavior up to temperatures of approximately 500K ($20a_0 \times 20a_0 \times 20a_0$) or 1000K ($30a_0 \times 30a_0 \times 30a_0$)
- From that temperature onwards, all meshes remain insensitive to temperature, resulting in zero thermal expansion coefficients.
- Generally, increasing coarsening results in a more pronounced thermal contraction. Cluster size has little or no effect for low values of n'_h, while large variations appear for coarse meshes. However, these variations are seemingly uncorrelated with the cluster size.

In other words, the thermal expansion behavior of coarse EAM Ta only likens that of the atomistic system for temperatures below 300K (which is known to be incorrect). At higher temperatures, the a_0-T simulations display very little structure and do not offer non-zero thermal expansion coefficients. Thus, there is no basis to carry out an analysis such as that presented in Fig. 8 for Al.

4.2.2. Thermal expansion from free-energy calculations in the quasiharmonic approximation. For consistency, however, we next calculate the thermal expansion coefficients α_{PBC} and α_{FS} for periodic and finite atomistic crystals within the quasiharmonic approximation. We study a periodic (infinite) $7a_0 \times 7a_0 \times 7a_0$ crystal containing 686 atoms, and a $12a_0 \times 12a_0 \times 12a_0$ finite crystal containing 3925 atom, which yields the largest possible diagonalizable dynamical matrix. Figure 16(a) shows the normalized eigenfrequency spectra for the periodic sample for several different lattice parameters. The results for the finite system are given in Fig. 16(b), where a shift to lower frequencies is observed as the lattice parameter is increased. Interestingly, the differences among the lattice parameters considered are much less pronounced than for the Al results shown in Fig. 9, which suggests a weaker volume (temperature) dependence.

As in Section 4.1.2, from these data we calculate α for Ta within the quasiharmonic approximation. This gives rise to constant thermal expansion coefficients of $\alpha_{\rm PBC} = 7.30 \times 10^{-7}$ and $\alpha_{\rm FS} = -2.42 \times 10^{-7}$ K^{-1}, respectively. These coefficients are substantially different than those corresponding to the periodic and finite systems in the temperature range where linearity is observed (1000 to 2000K). In fact, $\alpha_{\rm PBC}$ corresponds to a temperature of 364K for the MD system in Fig. 13, while $\alpha_{\rm FS}$ corresponds to temperatures of 531K and 497K for the 17261 and 56791-atom systems respectively, in the anomalous temperature region of the potential. This suggests that the quasiharmonic approximation is not a satisfactory one in the case of EAM Ta. Indeed, MacDonald and Shukla had already noted the difficulties to replicate the thermal expansion behavior of refractary metals such as Ta using atomistic calculations with central force potentials [68].

A quasiharmonic analysis of mesh and cluster effects in Ta, such as that performed for Al in Section 4.1.3, is therefore not warranted in this case, since not even the atomistic behavior is captured. We simply conclude that the thermal expansion behavior of EAM Ta displays a complex temperature dependence and that the quasiharmonic approximation is only valid in the low temperature regime, where EAM Ta behaves anomalously in any event. Of course, we do not discount other potentials for Ta (perhaps including angular terms [69], or fitted to thermal expansion data [70]) from offering a more satisfactory behavior for coarse meshes. However, an analysis of different interatomic potentials is not the subject of this work and we leave this comparison for future studies.

5. Discussion and conclusions

We have proposed a dynamic version of the Quasicontinuum method based on Brownian dynamics modeled via a Langevin equation. The resulting stochastic differential equation is integrated in time using Newmark's ($\beta = 0; \gamma = \frac{1}{2}$) method, which is seen to behave robustly even for very coarse meshes. The method reduces to full molecular dynamics in the atomistic limit and a system of strongly-coupled oscillators in the coarse limit. The main limitations are two, namely, (i) that the attainable time steps are bounded by the fastest nodal vibrations, which for atomistic systems can be of the order of fs, and (ii) that it contains no particular mechanism for suppressing wave reflections at mesh boundaries. The unphysically accumulated heat is dealt with

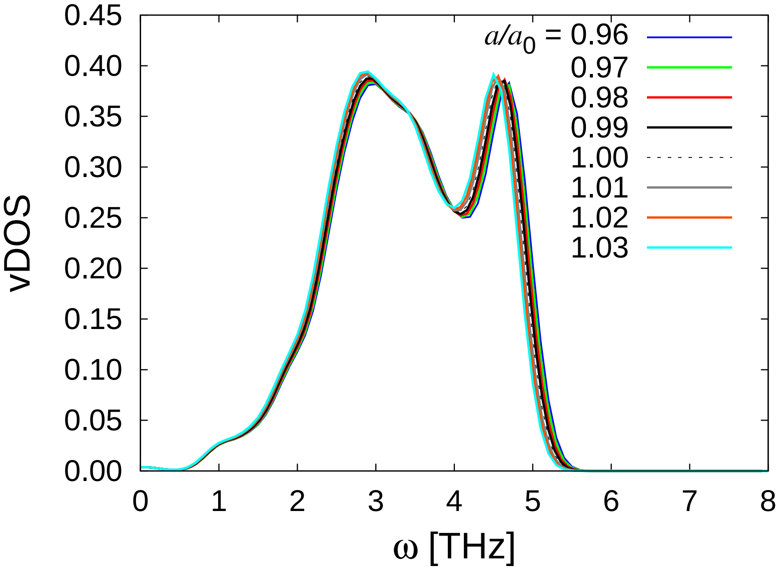

(a) Periodic system with 686 atoms representing bulk Ta

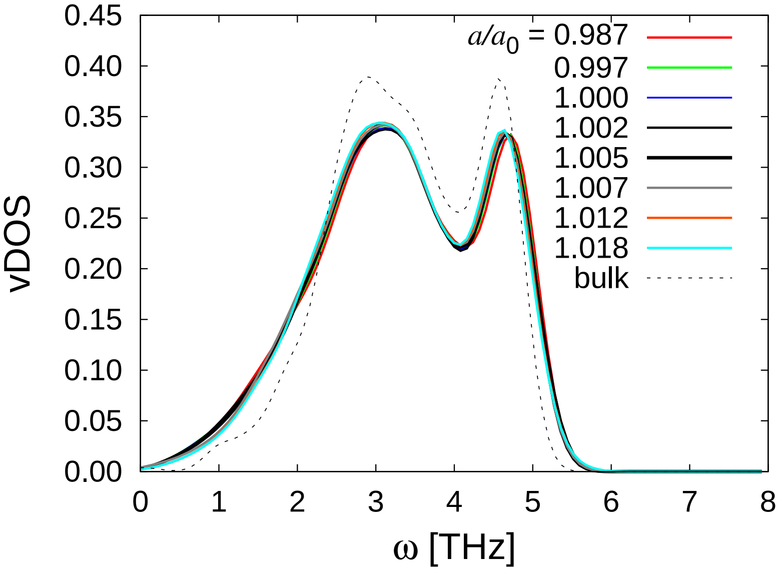

(b) Finite system containing 3925 atoms. Note how the band of allowable frequencies narrows with crystal expansion.

Figure 16. Normalized vDOS as a function of the normalized lattice parameter a/a_0 for cubic Ta crystallites with different boundary conditions. a_0 is 3.3026 Åfor an infinite system and 3.2782 Åfor our $12a_0 \times 12a_0 \times 12a_0 \times a_0$ finite crystal. The differences among the studied lattices are much more subtle than for Al (cf. Fig. 9).

explicitly by overdampening to maintain stable dynamics. Methods to increase the timestep in unstructured triangulations have been proposed. For example, Kane *et al* [40] and Lew *et al* [71] have developed a class of asynchronous variational integrators (AVI) for non-linear dynamics that permit the selection of independent time steps in each element. AVI are derived from a discrete form of Hamilton's variational principle, which makes the algorithm conserve its multisymplectic structure. These features make it an attractive integrator for dissipative mechanical systems in unstructured meshes. Coupling AVI to our dynamic QC framework could significantly enhance the extent of time scales probed during simulations where meshes are adaptively refined.

(Given the number of abnormalities attendant to EAM Ta, we omit it from the succeeding discussion). Our metric of choice to assess the entropic impoverishment of coarse meshes is the thermal expansion coefficient α. For fcc Al, our method recovers the atomic α —as given by the interatomic potential employed— in the atomistic limit, and produces coarse thermal expansion coefficients that obey the relation:

$$\alpha(n'_h) \approx \frac{1.53 \times 10^{-5}}{n'_h} \approx \frac{\alpha_{\mathrm{at}} N_h}{N} \tag{53}$$

This linear dependence with the number of nodes (or inverse with the mesh size) permits the use of rescaling coefficients to account for the loss of vibrational entropy. For example, to compute ensemble averages at temperature T in a mesh (N, N_h, r_c), one would first calculate the corresponding $\alpha(n'_h)$ from eq. (53); then, the equivalent temperature at which the said mesh would reproduce the full thermal behavior could be obtained by applying a rescaling of the type $T\alpha_{\mathrm{at}}/\alpha' = T'$.

The cluster size has no effect on dynamic simulations (cf. Fig. 8), only on static calculations, via V_0, which enters the formula to compute α as a normalization factor, eq. (51). The phenomenology of the cluster size effect on V_0 can be rationalized as follows. In dynamic simulations, the effect of the cluster size on the bulk nodes becomes smeared by thermal energy, *i.e.* the nodal kinetic energy washes out the subtle differences caused by the cluster size in the calculation of the forces. Surface nodes have higher energies than bulk nodes but, at finite temperatures, the differences due to the cluster size become smeared out as well. However, in static simulations the exposed surface that is not contained in any cluster (the internodal area beyond the cluster radii) has a higher energy than the surface represented/contained in the clusters. Therefore, the system will tend to 'shrink' these regions to minimize the energy. This *capillary* effect, only important at 0K, results in lower expansion volumes.

In the QC formulation considered here [20], nodal forces are computed from rigid clusters that do not contribute to the system's entropy. Therefore, entropic losses in coarse meshes are mainly due to a reduced configurational space. To mitigate this shortcoming, nodal forces could be calculated from the derivatives of the free energy at the cluster level, rather than just from the potential energy as in eq. (7). The free energy at the cluster level could be built assuming the quasi or local harmonic approximations [72] to pre-compute a set of Grüneisen paremeters to couple the normal frequencies to the deformation gradient from which cluster sites are interpolated. This is similar to finite-temperature quasistatic methods which build their free energy functionals from the underlying static lattice. However, these types of formulations typically rely on *macroscopic* averages, which are incompatible with Hamilton's equations, as has been discussed by Rodney [73].

While attempting to rationalize entropic losses in coarse QC meshes by using the quasiharmonic approximation, we have found that their vibrational densities of states display an unexpected behavior. Intuitively, coarser meshes give rise to narrower frequency spaces, a consequence of the incapacity of a coarse mesh to support short wavelength (high-energy) modes. In an homogeneous system, the short wavelength limit is dictated by the shortest nodal distance, which of course depends on the mesh size. However, for Al we have found that the vibrational spectra is hardest for intermediate coarsening meshes (cf. Fig. 11(b)). This effect cannot be explained using nodal mass arguments alone, as we have shown in Fig. 12(a). Instead, we have seen that this anomalous behavior is caused by the force constants (Fig. 12(b)). This may be an artifact caused by QC's intrinsic formulation, which we rationalize as follows. For homogeneous deformations, such as those induced by thermal expansion, crystal properties are independent of the mesh size. In such cases, eqs. (7) are only affected by the cluster size and the nodal weights n_h. Then, for a given cluster radius, it is the nodal weights that determine the magnitude of the nodal forces and, in turn, the force constants. However, as eq. (40) shows, when the cluster size is sufficently large to cause cluster overlap all weights are set to one. In such cases, eq. (41) simply becomes:

$$D_{\alpha\beta}(\boldsymbol{l},\boldsymbol{l}') = K_{\alpha\beta}(\boldsymbol{l},\boldsymbol{l}')/m_a$$

and the eigenfrequencies depend solely on the value of the force constants. In our Al $16a_0 \times 16a_0 \times 16a_0$ samples, for $r_c = 4$, cluster overlap can first occur for $N_h \sim 332$, consistent with the value where the force constants are maximum in Fig. 12(b) (at $N_h = 365$). From that point on, the force constants gradually decrease to their atomistic value.

This anomaly could be erradicated if n'_h, rather than n_h, were used as nodal weights. However, the set of $\{n_h\}$ ensures that summation rules are exact for all shape functions in eq. (4) and they cannot be altered. In any case, this anomalous behavior is not transmitted to the quasiharmonic calculation of thermal expansion coefficients, which are consistent with those obtained via fully-dynamical QC simulations. In any case, an interesting exercise outside the scope of this paper would be to study wave transmission from atomistic domains into coarser regions. Conceivably, the reflection of fine-scale vibrations at these boundaries could become suppressed if it is confirmed that coarse domains within our dynamic QC framework can support them. This is only speculation, of course, as a detailed study of transmissions/reflections across inhomogeneous boundaries should be performed.

We finish by pointing out that the interest in a finite-temperature extension of QC mainly resides in the fact that the zero-temperature Quasicontinuum method has been widely used to study diverse problems (see Section 1 for details). Therefore, our intention with this work was not simply to add yet another dynamic atomistic/continuum-bridging method to the catalog of available methodologies, but to provide a dynamic generalization to a technique which has been applied to many problems of interest. In this sense, our method stands next to techniques such as MD/CADD [18], which is has also been used widely (see Curtin and Miller [2], and references therein). However, a few differences exist between dynamic QC and MD/CADD. For example, in our method the non-atomistic region is fully dynamic, whereas it remains quasistatic in MD/CADD. Because of this, α appears naturally in QC (fully anharmonic), while in MD/CADD it has to be imposed externally. Another difference pertains to the utilization of the damping coefficient: in MD/CADD, ν is gradually ramped from zero in the coarse region to ν_{at} at the atomistic boundary; in QC each node is automatically assigned a viscosity commensurate with its mass.

6. Acknowledgments

This work performed under LDRD project Project 06-SI-005 under the auspices of the US Department of Energy by Lawrence Livermore National Laboratory under contract DE-AC52-07NA27344. GV and MO gratefully acknowledge the support of the Department of Energy through Caltech's PSAAP Center for the Predicitive Simulation of the Dynamic Response of Materials.

Appendix: Derivation of the free energy expression.

We start from the expression for the partition function of a system of distinguishable particles, eq. (45):

$$Z_h(\theta,T) = \frac{1}{(2\pi\hbar)^{3N_h}} \int_X \exp\Big\{ - \frac{H_h(\boldsymbol{q}_h,\boldsymbol{p}_h,\theta)}{k_B T}\Big\} d\boldsymbol{q}_h d\boldsymbol{p}_h \tag{A.1}$$

Integration over momenta can be separated out from eq. (A.1), giving:

$$Z_h(\theta,T) = \left(\frac{m_h k_B T}{2\pi\hbar^2}\right)^{3N_h/2} \int_X \exp\Big\{ - \frac{\Phi_h(\boldsymbol{q}_h,\theta)}{k_B T}\Big\} d\boldsymbol{q}_h \tag{A.2}$$

Hence, the free energy of the system is:

$$\begin{aligned} F_h(\theta,T) &= -k_B T \ln Z(\theta,T) = \\ &= -k_B T \left(\ln \int_X \exp\Big\{ - \frac{\Phi_h(\boldsymbol{q}_h,\theta)}{k_B T}\Big\} d\boldsymbol{q}_h + \frac{3N_h}{2} \ln \frac{m_h k_B T}{2\pi\hbar^2} \right) \end{aligned} \tag{A.3}$$

To find solutions of the *configuration integral* in the first term of the r.h.s. of (A.3) we assume for Φ the harmonic form introduced in eq. (34):

$$\Phi_h(\boldsymbol{u}_h,\theta) \approx \Phi_h(\boldsymbol{0},\theta)) + \frac{1}{2} \sum_{\boldsymbol{l}_h} \sum_{\boldsymbol{l}'_h} D_{\alpha\beta}(\boldsymbol{l}_h,\boldsymbol{l}'_h)|_{\boldsymbol{0}}\, \boldsymbol{u}_h(\boldsymbol{l}_h) \boldsymbol{u}_h(\boldsymbol{l}'_h) \tag{A.4}$$

where both the zero-th and second order terms are evaluated in equilibrium (configurational state $\mathbf{0}$). Equation (A.3) then becomes:

$$F_h(\theta,T) \approx -k_BT\left(\frac{3N_h}{2}\ln\frac{m_hk_BT}{2\pi\hbar^2}+\right.$$
$$\left.+\ln\int_X \exp\left\{-\frac{\Phi_h(\mathbf{0},\theta)+\frac{1}{2}\sum\sum D_{\alpha\beta}(\mathbf{0})\boldsymbol{u}_h\boldsymbol{u}'_h}{k_BT}\right\}d\boldsymbol{u}_h\right) \quad \text{(A.5)}$$

where, for clarity, we have simplified the notation by ommitting the dependence on $\boldsymbol{l}_h$ and eliminating running indices from the summations. The configuration integral can be simplified by applying the logarithm:

$$F_h(\theta,T) \approx -k_BT\left(\frac{3N_h}{2}\ln\frac{m_hk_BT}{2\pi\hbar^2}-\frac{\Phi_h(\mathbf{0},\theta)}{k_BT}+\right.$$
$$\left.+\ln\int_X \exp\left\{-\frac{\frac{1}{2}\sum\sum D_{\alpha\beta}(\mathbf{0})\boldsymbol{u}_h\boldsymbol{u}'_h}{k_BT}\right\}d\boldsymbol{u}_h\right) \quad \text{(A.6)}$$

By virtue of eq. (37), the double sum in eqs. (A.5) and (A.6) can be replaced with a single product when the transformation matrix is diagonal, *i.e.* eq. (A.6) can be reduced to:

$$F_h(\theta,T) \approx \Phi_h(\mathbf{0},\theta)-k_BT\left(\frac{3N_h}{2}\ln\frac{m_hk_BT}{2\pi\hbar^2}+\right.$$
$$\left.+\ln\int_X\prod_i^{3N_h}\exp\left\{-\frac{{\omega_i}^2{u_i}^2}{2k_BT}\right\}du_i\right) \quad \text{(A.7)}$$

After performing the change of variable $x_i = \omega_i(\theta)u_i/\sqrt{2k_BT}$ and converting the logarithm of a product into a sum of logarithms, the integral becomes:

$$F_h(\theta,T) \approx \Phi_h(\mathbf{0},\theta)-k_BT\left(\frac{3N_h}{2}\ln\frac{m_hk_BT}{2\pi\hbar^2}+\right.$$
$$\left.+\sum_i^{3N_h}\ln\left\{\frac{\sqrt{2k_BT}}{\omega_i(\theta)}\int_X\exp\left(-{x_i}^2\right)dx_i\right\}\right) \quad \text{(A.8)}$$

where the term inside the logarithm is simply a *Gaussian* integral, which integrated over the entire configurational space ($\int_X \equiv \int_{-\infty}^{\infty}$) is $\sqrt{\pi}$. Thus:

$$F_h(\theta,T) \approx \Phi_h(\mathbf{0},\theta)-k_BT\left(\frac{3N_h}{2}\ln\frac{m_hk_BT}{2\pi\hbar^2}+\sum_i^{3N_h}\ln\left\{\frac{\sqrt{2\pi k_BT}}{\omega_i(\theta)}\right\}\right) \quad \text{(A.9)}$$

Decomposing the last term into a sum of logarithms, we arrive at:

$$F_h(\theta,T) \approx \Phi_h(\mathbf{0},\theta) - k_BT\Bigg(\frac{3N_h}{2}\ln\frac{m_hk_BT}{2\pi\hbar^2} + \\ + 3N_h\ln\sqrt{2\pi k_BT} - \sum_i^{3N_h}\ln\left\{\omega_i(\theta)\right\}\Bigg) \quad \text{(A.10)}$$

and:

$$F_h(\theta,T) \approx \Phi_h(\mathbf{0},\theta) - k_BT\left(\frac{3N_h}{2}\left(\ln\frac{m_hk_BT}{2\pi\hbar^2} + \ln 2\pi k_BT\right) - \sum_i^{3N_h}\ln\left\{\omega_i(\theta)\right\}\right) \quad \text{(A.11)}$$

which, after operating slightly, is the final form for the free energy given in eq. (46)

References

[1] Ortiz, M., Cuitiño, A. M., Knap, J. & Koslowski, M., MRS Bulletin 26 (2001) 16

[2] Curtin, W. A. & Miller, R. E., Modelling and Simulation in Materials Science and Engineering 11 (2003) R33

[3] Medina, F. & Rosales, F., Engineering Computations 4 (1987) 139

[4] Rudd, R. E. & Broughton, J. Q., Physical Review B 72 (2005) 144104

[5] Cathers, B, Bates, S, & O'Connor, BA, International Journal for Numerical Methods in Fluids 9 (1989) 783

[6] Jiang, L, & Rogers, RJ, Communications in Applied Numerical Methods 7 (1991) 595

[7] Von Neumann, J. & Richtmyer, R. D., J. Appl. Phys. 21 (1950) 232

[8] Cai, W., de Koning, M., Bulatov, V. V. & Yip, S., Physical Review Letters 85 (2000) 3213

[9] E, W. & Zhongyi, H., Physical Review Letters 87 (2001) 135501

[10] Park, H. S., Karpov, E. G., Liu, W. K. & Klein, P. A., Philosophical Magazine 85 (2005) 79

[11] Curtaloro, S. & Ceder, G., Physical Review Letters 88 (2002) 255504

[12] Wagner, G. J., Jones, R. E., Templeton, J. A. & Parks, M. L., Computer Methods in Applied Mechanics and Engineering 197 (2008) 3351

[13] Shenoy, V., Shenoy, V. & Phillips, R., Mater. Res. Soc. Symp. Proc., vol. 538 (1999), pp. 465-471

[14] Wu, Z.-B., Diestler, D. J., Feng, R. & Zeng, X. C., Journal of Chemical Physics 111 (2003) 8013

[15] Dupuy, L. M., Tadmor, E. B., Miller, R. E. & Phillips, R., Physical Review Letters 95 (2005) 060202

[16] Tang, Z., Zhao, H., Li, G. & Aluru, N. R., Physical Review B 74 (2006) 064110

[17] Kulkarni, Y., Knap, J. & Ortiz, M., Journal of the Mechanics and Physics of Solids 56 (2008) 1417

[18] Qu, S., Shastry, V., Curtin, W. A. and Miller, R. E., Modelling and Simulation in Materials Science and Engineering 13 (2005) 1101

[19] Tadmor, E. B., Ortiz, M. & Phillips, R., Philosophical Magazine A 73 (1996) 1529.

[20] Knap, J. & Ortiz, M., Journal of the Mechanics and Physics of Solids 49 (2001) 1899.

[21] LeSar, R., Najafabadi, R. & Srolovitz, D. J., Physical Review Letters 63 (1989) 624

[22] Althoff, J. D., Morgan, D., De Fontaine, D., Asta, M., Foiles, S. M. & Johnson, D. D., Computational Materials Science 10 (1998) 411

[23] Baranyai, A. & Evans, D., Molecular Physics 74 (1991) 353

[24] Knap, J., Marian, J. & Ortiz, M., *Mesh optimization for the Quasicontinuum method: a generalization of VALE*, presented at the 21st International Congress on Theoretical and Applied Mechanics (ICTAM), Warsaw (Poland), 15-21 August 2004.

[25] Knap, J. & Ortiz, M., Physical Review Letters 90 (2001) 226102

[26] Marian, J., Knap, J. & Ortiz, M., Physical Review Letters 93 (2004) 165503

[27] Marian, J., Knap, J. & G. H. Campbell, Acta Materialia 56 (2008) 2389

[28] Marian, J. & Knap, J., International Journal for Multiscale Computational Engineering 5 (2007) 287

[29] Vujanovic, B. D. & Jones, S. E., "Variational methods in nonconservative phenomena", Mathematics in science and engineering v. 182 (Academic Press, San Diego, CA, 1989)

[30] Eringen, A. C. & Suhubi, E. S.. "Elastodynamics", Vol. 1 (Academic Press, New York, 1974).

[31] Hughes, T. J. R., "The Finite Element Method" (Dover Publications, New York, NY, 2000)

[32] Coffey, W. T., Kalmykov, Yu P. & Waldron, J. T., "The Langevin Equation", World Scientific Series in Contemporary Chemical Physics - Vol. 14 (World Scientific, Singapore, 2004)

[33] Kirkwood, J. G., Journal of Chemical Physics 3 (1935) 300.

[34] Gardiner, C. W., "Handbook of Stochastic Methods", 3rd ed. (Springer, New York, 2003).

[35] Kubo, R., Reports on Progress in Physics 29 (1966) 255.

[36] Leimkuhler, B., & Reich, S., "Simulating Hamiltonian Dynamics" (Cambridge University Press, Cambridge, UK, 2005)

[37] Melchionna, S., Journal of Chemical Physics 127 (2007) 044108

[38] Newmark, N. M., ASCE Journal of the Engineering Mechanics Division (1959) p. 167.

[39] Simo, J. C., Tarnow, N. & Wong, K. K., Computer Methods in Applied Mechanics and Engineering 100 (1992) 63

[40] Kane, C., Marsden, J. E., Ortiz, M. & West, M., International Journal for Numerical Methods in Engineering 49 (2000) 1295

[41] Courant, R., Friedrichs, K. & Lewy, H., IBM Journal, March 1967, pp. 215-234

[42] Zhang, G., & Schlick, T., Journal of Chemical Physics 101 (1994) 4995

[43] Bussi, G. & Parrinello, M., Physical Review E 75 (2007) 056707

[44] Nilsson, L. G. & Padro, J. A., Molecular Physics 71 (1990) 355

[45] Helfand, E., The Bell System Technical Journal 58 (1979) 2289

[46] Greenside, H. S., & Helfand, E., The Bell System Technical Journal 60 (1981) 1927

[47] Box, G. E. P. & Muller, M. E., The Annals of Mathematical Statistics 29 (1958) 610

[48] Biswas, R. & Hamann, D. R., Physical Review B 34 (1986) 895

[49] Kittel, C., "Introduction to Solid State Physics", 7th Ed. (Wiley, Hoboken, NJ, 1996)

[50] Maradudin, A. A., Montroll, E. W. & Weiss, G. H., "Theory of Lattice Dynamics in the Harmonic Approximation", in: Solid State Physics, Suppl. 3 (Academic Press, New York, NY, 1963)

[51] Cole, H., IBM Journal, April 1959, p. 126

[52] MacDonald, R. A., Physical Review B 5 (1972) 4139

[53] Hill, T. L., "An Introduction to Statistical Thermodynamics" (Dover Publications, New York, NY, 1986)

[54] Grimvall, G., "Thermophysical Properties of Materials", in *Selected Topics in Solid State Physics*, vol. XVIII, E. P. Wohlfarth (ed.) (North-Holland, Amsterdam, The Netherlands, 1986)

[55] International Tables for Crystallography (2006). Vol. D: Physical properties of crystals (Section 1.4.2), A. Authier, ed. (International Union of Crystallography, 2006)

[56] Srivastava, G. P., "The Physics of Phonons" (Taylor & Francis, New York, NY, 1990)

[57] Ho, C. Y., & Taylor, R. E., "Thermal Expansion of Solids" (ASM International, 1998)

[58] Maranganti, R. & Sharma, P., Journal of the Mechanics and Physics of Solids 55 (2007) 1823

[59] Diethelm, K., Ford, N. J., Freed, A. D. and Luchko, Y., Computer Methods in Applied Mechanics and Engineering 194 (2005) 743

[60] Touloukian, Y. S., Kirby, R. K., Taylor, R. E., and Lee, T. Y. R., "Thermal Expansion of Non-metallic Solids", in Thermophysical Properties Matter, vol. 13 (Plenum Publishing Co., New York, NY, 1977)

[61] Biegalski, M. D., Haeni, J. H., Trolier-McKinstry, S. & Schlom, D. G., Journal of Materials Research 20 (2005) 952

[62] Born, M. & Huang, K., "Dynamical Theory of Crystal Lattices" (Oxford University Press, Oxford, UK, 1956)

[63] Ercolessi, F. & Adams, J. B., Europhysics Letters 26 (1994) 583

[64] Liu, X-Y., Ercolessi, F. & Adams, J. B., Modelling and Simulations in Materials Science and Engineering 12 (2004) 665

[65] Pearson, W. B., "A Handbook of Lattice Spacings and Structures of Metals and Alloys" (Pergamon, New York, NY, 1958)

[66] Szeftel, J., Surface Science 152/153 (1985) 797

[67] Li, Y., Siegel, D. J., Adams, J. B. and Liu, X-Y., Physical Review B 67 (2003) 125101

[68] MacDonald, R. A. & Shukla, R. C., Physical Review B 32 (1985) 4961

[69] Mishin, Y, and Lozovoy, AY, Acta Materialia 54 (2006) 5013

[70] Ozaki, K, Fukutani, A, and Honda, K, JSME International Journal 44 (2001) 199

[71] Lew, A., Marsden, J. E., Ortiz, M. & West, M., Archive for Rational Mechanics and Analysis 167(2) (2003) 85

[72] Foiles, F. M., Physical Review B 49 (1994) 14930

[73] Rodney, D., in *Proceedings of the NATO Conference: "Thermodynamics, Microstructures and Plasticity"*, Eds. A. Finel, D. Maziera and M. Veron (Kluwer, Dortrecht, 2003)